DESIGNING AND ANALYSIS OF SOFC OPERATING WITH SYNGAS AND COAL GASIFICATION INTEGRATED SYSTEM

by

Can Gökhun Şekerci

B.S, Chemistry, Boğaziçi University, 2012

Submitted to the Institute for Graduate Studies in
Science and Engineering in partial fulfillment of
the requirements for the degree of
Master of Science

Graduate Program in Chemistry

Boğaziçi University

2015

DESIGNING AND ANALYSIS OF SOFC OPERATING WITH SYNGAS AND COAL GASIFICATION INTEGRATED SYSTEM

APPROVED BY:

Assist. Prof. Oktay Demircan (Thesis Supervisor)	.....
Prof. Naz Zeynep Atay	.....
Assoc. Prof. Selmiye Alkan Gürsel	.....

DATE OF APPROVAL: 23.07.2015

This thesis is dedicated to my parents
for their love, endless support and encouragement.

ACKNOWLEDGEMENTS

This study is financially supported by Boğaziçi University-BAP, Project No: 7440. I would like to address my special thanks to Chemistry Department of Boğaziçi Univeristy. I wish to thank Assist. Prof. Oktay Demircan for his supervision and challenging encouragement towards learning.

I also would like to thank my thesis committee members Assoc. Selmiye Alkan Gürsel and Prof. Naz Zeynep Atay for sparing their valuable time and reviewing my dissertation.

Eventually, my highest appreciation is addressed to my family: my mother, Harika Şekerci for teaching me self-discipline, my father, Kadri Okan Şekerci for the insight of free spirit, my uncle and his wife, MD. MSc. Aziz Gürhan Birler and Prof. Sema Birler for their encouragement and inspirational previous work.

ABSTRACT

DESIGNING AND ANALYSIS OF SOFC OPERATING WITH SYNGAS AND COAL GASIFICATION INTEGRATED SYSTEM

Solid oxide fuel cells (SOFCs) are electrochemical conversion devices transforming chemical energy of fuel into electric current with high efficiency. SOFCs are composed of three main parts: anode, cathode, and electrolyte. High operating temperature provides fuel flexibility to SOFCs due to employing oxide ions as charge carrier. Even though, high operating temperature of SOFCs causes material and fabrication restrictions, it enables the utilization of coal syngas as fuel. Internal reforming of methane could be achieved in the anode compartment of SOFC due to the high operating temperature. In this study the SOFC operating with syngas and coal gasification integrated system is designed and developed to investigate the effects of fuel concentration on the SOFCs' performance. Different fuel concentrations of H_2 and CH_4 are fed to SOFC test rig and fuel monitoring system employing mid-IR absorption spectroscopy. Electrochemical performance characterization and $in-situ$ SOFC exhaust analysis conclude that H_2 has a better fuel performance than CH_4 with respect to open circuit voltage (OCV) and power output values. Furthermore, CH_4 is promising for the integration of coal gasification system with a solid oxide fuel cell (SOFC) for clean coal utilization. The fuel conversion efficieny of SOFC system operating at 500 mV anodic overpotential with the fuel of 50 sccm CH_4 is calculated as 18.57 %.

ÖZET

SENTEZ GAZI İLE ÇALIŞAN KATI OKSİT YAKIT HÜCRESİ VE KÖMÜR GAZLAŞTIRMA ENTEGRE SİSTEMİ DİZAYN VE ANALİZİ

Katı Oksit Yakıt Hücreleri (KOYH) yakıtın kimyasal enerjisini elektrik akımına yüksek verimlilik ile dönüştüren elektrokimyasal dönüştürücü cihazlardır. KOYH sistemleri anot, katot ve elektrolit olmak üzere üç ana parçadan oluşur. Yüksek çalışma sıcaklıkları ve yük taşıyıcı olarak oksit iyonlarının görev alıyor olması KOYH sistemlerinde yakıt esnekliği sağlar. KOYH sistemlerinin yüksek çalışma sıcaklıkları, malzeme ve üretim kısıtlamarına sebep olsa da kömür üstü sentez gazının yakıt olarak kullanılmasına olanak sağlar. Metan gazının dahili iyileştirilmesi KOYH sisteminin anot kompartmanında yüksek çalışma sıcaklıkları sayesinde gerçekleşir. Bu çalışmada, farklı yakıt derişimlerinin KOYH performansına olan etkilerini araştırmak amacı ile sentez gazı ile çalışan KOYH ve kömür gazlaştırma entegre sistemi dizayn ve kurulumu gerçekleştirilmiştir. KOYH test sistemi ve absorpsiyon spektroskopisi uygulayabilen yakıt ölçüm sistemi farklı konsantrasyonlarda H_2 ve CH_4 ile beslenmiştir. Elektrokimyasal performans ve simultane KOYH egzoz analizleri, üstün açık devre gerilimi ve güç değerleri ile H_2'nin CH_4'e göre daha iyi bir yakıt olduğunu göstermektedir. Ayrıca, CH_4 yakıtının dönüşüm değerleri KOYH sistemlerinin kömür gazlaştırma sistemleri ile entegre edilmesi açısından umut vericidir. 500 mV anodik potansiyel ile çalıştırılan ve 50 sccm CH_4 ile beslenen KOYH sisteminin yakıt dönüşüm verimliliği % 18,57'dir.

TABLE OF CONTENTS

ACKNOWLEDGEMENTS iv
ABSTRACT v
ÖZET vi
LIST OF FIGURES ix
LIST OF TABLES xii
LIST OF SYMBOLS xiii
LIST OF ACRONYMS/ABBREVIATIONS xiv
1. INTRODUCTION 1
1.1. Fuel Cells 2
1.2. Solid Oxide Fuel Cells (SOFCs) 4
1.3. Materials 5
1.3.1. Anode 6
1.3.2. Electrolyte 7
1.3.3. Cathode 8
1.4. Characterization and Analysis 9
1.4.1. Electrochemistry 9
1.4.2. Analytical Characterization 14
1.5. Fuel Types 15
1.6. Fuel Conditioning and Monitoring 16
1.7. Scope of the Thesis 19
2. Experimental 21
2.1. Experimental setup 21
2.1.1. Preperation of The MEA and SOFC Stack Design 21
2.1.2. SOFC Test Rig 23
2.1.3. Fuel Monitoring System 24
2.2. Characterization 28
2.2.1. Electrochemical Characterization 28
2.2.2. $In-situ$ SOFC Exhaust Analysis 29
3. RESULTS 32

3.1. Electrochemical Performance 32
3.2. $In-situ$ SOFC Exhaust Analysis 46
4. CONCLUSIONS 53
5. FUTURE WORKS 55
REFERENCES 56

LIST OF FIGURES

Figure 1.1. Schematic representation of SOFC operation. 4

Figure 1.2. Schematic representation of yttria, Y_2O_3, stabilized zirconia, ZrO_2, (YSZ). 8

Figure 1.3. Schematic graph of the voltage drop of SOFC as a function of withdrawn current density, a) low current regime, b) medium current regime, and c) high current regime. 10

Figure 1.4. Schematic representation of EIS Nyquist plot. 14

Figure 1.5. Calculated transmission spectra of involved gas species. 18

Figure 2.1. Gold paste application on the surface of the membranes. 21

Figure 2.2. Gold mesh at the bottom of cathode layer. 22

Figure 2.3. Gold mesh on the top of anode layer. 22

Figure 2.4. Bipolar seperating plates. 22

Figure 2.5. SOFC stack in the SOFC test rig. 23

Figure 2.6. Experimental setup of SOFC Test Rig. 24

Figure 2.7. Schematic representation of optical allignment of the fuel monitoring system. 25

Figure 2.8. Schematic representation of applied square signal to drive the LEDs. 26

Figure 2.9. Picture of fuel monitoring system. 27

Figure 2.10. Heating program for SOFC operation. 29

Figure 2.11. Calibration curve for CH_4 with LED2350. 30

Figure 3.1. Performance curves of SOFC running with H_2 flowing at the rate of 100 sccm (blue), 200 sccm (red), and 300 sccm (green). 33

Figure 3.2. Performance curves of SOFC running with H_2 flowing at the rate of 200 sccm (red) and CH_4 flowing at the rate of 50 sccm (blue), and 100 sccm (green). 34

Figure 3.3. Maximum power density values for different fuel concentrations at different stages of measurements. 37

Figure 3.4. Nyquist plots of electrochemical impedance spectroscopy for 100 sccm H_2 at OCV (dark blue), at 100 mV overpotential (orange), at 200 mV overpotential (light blue), and at 300 mV overpotential (purple). 38

Figure 3.5. Nyquist plots of electrochemical impedance spectroscopy for 200 sccm H_2 at OCV (dark blue), at 100 mV overpotential (orange), at 200 mV overpotential (light blue), and at 300 mV overpotential (purple). 39

Figure 3.6. Nyquist plots of electrochemical impedance spectroscopy for 300 sccm H_2 at OCV (dark blue), at 100 mV overpotential (orange), at 200 mV overpotential (light blue), and at 300 mV overpotential (purple). 40

Figure 3.7. Nyquist plots of electrochemical impedance spectroscopy for 50 sccm CH_4 at OCV (dark blue), at 100 mV overpotential (orange), at 200 mV overpotential (light blue), and at 300 mV overpotential (purple). 41

Figure 3.8. Nyquist plots of electrochemical impedance spectroscopy for 100 sccm CH_4 at OCV (dark blue), at 100 mV overpotential (orange), at 200 mV overpotential (light blue), and at 300 mV overpotential (purple). 42

Figure 3.9. Polarization resistance corrected EIS measurements. 43

Figure 3.10. Polarization resistance corrected EIS measurements. 44

Figure 3.11. $In-situ$ monitoring for 50 sccm CH_4 fuel feed with LED2350 under operating conditions of SOFC. 47

Figure 3.12. $In-situ$ monitoring for 100 sccm CH_4 fuel feed with LED2350 under operating conditions of SOFC. 48

Figure 3.13. $In-situ$ concentration monitoring for 50 sccm CH_4 fuel feed with respect to exhaust gas analysis. 49

Figure 3.14. $In-situ$ concentration monitoring for 100 sccm CH_4 fuel feed with respect to exhaust gas analysis. 51

LIST OF TABLES

Table 1.1. Types of fuel cells. 3

Table 3.1. Open circuit voltage values (V) for different fuel concentrations. . . 35

Table 3.2. Maximum power values (W/cm^2) for different fuel concentrations. 36

Table 3.3. Bulk resistance values (Ω cm^2) for different fuel concentrations. . . 46

LIST OF SYMBOLS

A	Absorption
F	Faraday Constant
I	Transmitted Intensity
I_0	Incident Intensity
J	Current Density
J_0	Exchange Current Density
R_b	Bulk Resistance
R_p	Polarization Resistance
R_T	Total Resistance
T	Transmittance
V	Voltage
Vpp	Peak to Peak Voltage
V_{rev}	Reversible Cell Voltage
Z	Impedance
Z_{im}	Imaginary Impedance
Z_{real}	Real Impedance
α	Transfer Coefficient
ε	Absorptivity
ϕ	Phase Difference
ω	Relaxation Frequency
ΔG	Gibb's Free Energy
Δj	Alternating Current
ΔV	Alternating Voltage

LIST OF ACRONYMS/ABBREVIATIONS

AFC	Alkaline Fuel Cell
AFM	Atomic Force Microscopy
EIS	Electrochemical Impedance Spectroscopy
FC	Fuel Cell
GDC	Gadalinium Doped Ceria
HITRAN	High Resolution Transmission
IR	Infrared
LED	Ligth Emitting Diode
LSCo	Stronium-Doped Lanthanum Cobaltite
LSM	Lanthanum Strontium Manganite
LSF	Stronium-Doped Lanthanum Ferrite
LSM	Lanthanum Strontium Manganite
LSZ	Stronium-Doped Lanthanum Zirconate
LSV	Linear Sweep Voltammetry
MEA	Membrane Electrode Assembly
MCFC	Molten Carbonate Fuel Cell
OCV	Open Circuit Voltage
PAFC	Phosphoric Acid Fuel Cell
PEM	Polymer Electrode Membrane Fuel Cell
SEM	Scanning Electron Microscopy
SOFC	Solid Oxide Fuel Cell
TPB	Triple Phase Boundry
XPS	X-ray Photoelectron Spectroscopy
XRD	X-ray Diffraction
YSZ	Yittria Stabilized Zirconia

1. INTRODUCTION

Energy is one of the basic needs of our era. And this need will continue to grow rapidly with the improvement of technology and increasing population. Most of the energy produced to satisfy this need is fulfilled from fossil fuels. Increasing need of energy, consumption of natural resources and the enviromental effect of the exhaust gases formed increased the attention of the resarchers to alternative energy production methods. Because of the harmful side effects of using fossil fuels, researchers are focused on sustainable and clean energy conversion devices such as solar panels and wind turbines. Since coal maintains being the most common energy resource in the world, development of clean, enviromentally friendly coal technologies with high efficiency with zero emission is necessary.

Conventional energy production methods using coal as resource are not efficient. The Carnot cycle restricts the efficiency of these methods to 35 % since a conversion to mechanical energy is involved [1]. Moreover, exhaust gases formed during these processes are severely harmful to the environment and ecosystem. Therefore, there is a huge need for new energy production methods in which coal can be utilized with high efficiency and without toxic gas realease.

Instead of employing burning technologies to produce electricity, electrochemical conversion of chemical fuel (coal) into electricity can be considered. Fuel Cells (FC) are the most promising electrochemical converters in this manner since electrochemical conversion process of fuel into electricity via fuel cells is not restricted by Carnot cycle. Among the variety of fuel cells, Solid oxide fuel cells (SOFCs) step up with their high efficiency up to 60 % and fuel flexibility [2]. It is possible for SOFCs to utilize several kinds of hydrocarbons as fuel, such as coal syngas derived from coal gasification. Thus, SOFCs are believed to become pioneers in clean and enviromentally friendly coal technology for energy production [3].

1.1. Fuel Cells

Fuel cell is an electrochemical conversion device composed of three basic components; anode, electrolyte and cathode. Fuel cells convert chemical potential of the fuel into electrical power through electrochemical processes. A great range of fossil fuels and hydrocarbons can be utilized as fuel on fuel cells. Formation of hydrogen and oxygen ions; by the oxidation of hydrogen gas at anode compartment and reduction of oxygen gas to oxide ions at cathode compartment; and migration of these ions from cathode to anode or vice versa with the help of an ion conducting electrolyte enables the conversion of chemical potential of fuel into electrical power.

Fuel cells are known and appreciated for their higher efficiency. Although, the efficiency of the fuel cells are not constricted by the 'Carnot Cycle', some limiting factors like ohmic losses, electrode overpotentials, concentration losses and general losses due to the exterior materials used in the cell assembly restrict the theoretical efficiency to 65 % [4]. Ohmic losses include the resistance caused by the MEA materials and the cell geometry. Electrode overpotentials are related with the activation polarization and concentration losses are proportional with the concentration change of the fuel gases during the operation of the SOFCs.

Although, the idea of converting chemical fuels directly into electricity is first proposed by Nernst and his colleagues [5] at the end of the nineteenth century, the procedure is firstly discovered by William Robert Crove in 1830s. William Robert Crove produced hydrogen and oxygen from water by using two platinium electrodes. Then in 1839, he reversed the process to combine two elements and produce an electric current, the very first fuel cell [6]. But back in nineteenth century, electrical conduction was not clear yet and there was a little information about the electron. Electronic conductivity used to be achieved by metals and aquous ionic solutions according to ohm's law. It was thought that the conductivity was just electrical. Then, Nernst realized that metal oxides (zirconia) become electronically and ionicaly conductive depending on the temperature [7]. The first fuel cell concept based on zirconium oxide was introduced in the late 1930s by Baur and Preis. [8]. The commercialization of fuel cells was not

Table 1.1. Types of fuel cells.

Name	Electrolyte	Charge Carrier Ion	Fuel Type	Operation Temperature
Alkaline Fuel Cell	KOH	OH^-	Pure H_2	50-200 ^{0}C
Polymer Electrolyte Membrane Fuel Cell	Polymer (Nafion)	H^+	Pure H_2 and ethanol	50-100 ^{0}C
Phosphoric Acid Fuel Cell	H_3PO_4	H^+	CO free H_2	200-220 ^{0}C
Molten Carbonate Fuel Cell	Li_2CO_3 + K_2CO_3	$CO_3{}^{2-}$	H_2, hydrocarbons	600-650 ^{0}C
Solid Oxide Fuel Cell	YSZ	O^{2-}	H_2, hydrocarbons	650-100 ^{0}C

until the 1950s. When the American space program Apollo started to use fuel cells, it became a growing and attractive research area.

There are five main types of fuel cells named according to their electrolyte materials. These are 'Alkaline Fuel Cell (AFC)', 'Polymer Electrolyte Membrane Fuel Cell (PEM)', 'Phosphoric Acid Fuel Cell (PAFC)', 'Molten Carbonate Fuel Cell (MCFC)' and 'Solid Oxide Fuel Cell (SOFC)'. Each type of fuel cells have diffrent characterstics, such as electrolyte efficiency, operation temperature, charge carrier ion and fuel composition. Types of fuel cells and their characteristics can be seen from Table 1.1. First three types of these fuel cells are poor according to their fuel need since they need pure hydrogen gas. To obtain pure hydrogen gas an external fuel reforming step is necessary. But MCFCs and SOFCs can operate with a direct feed of gasified hydrocarbons. Although, both fuel cells are proper for vast range of fuel types, SOFCs step up with the electrolyte material, Yittria stabilized Zirconia (YSZ). YSZ exhibits necessary mechanical and electrochemical properties at the high operating temperatures of SOFCs. The high ionic conductivity and the low electronic conductivity, which is essential for an electrolyte material, is achieved by doping Zirconia (ZrO_2) with Yittria (Y_2O_3). This enables the fluorite-type crystal structure of ZrO_2 to become stable at room temperature and creates vacancies for the charge carrier ion through the crystal

structure [9, 10].

1.2. Solid Oxide Fuel Cells (SOFCs)

Solid Oxide Fuel Cells (SOFCs) are generally composed of an metal oxide electrolyte covered by two porous electrodes at both sides. First SOFC was developed by Baur and Preis at 1937 after Nernst discovered that metal oxides can be both ionically and electronicaly conductive [7]. The prior advantage of the SOFC is the fuel flexibility. The charge carrier ion in the membrane electrode assembly (MEA) is the oxide ion, O^{2-}, which has the property of oxidizing H_2 and CO. Also the high operating temperatures of SOFCs put away the necessity of an external fuel reforming step for hydrocarbons before used as fuel. Thus, fossil fuels including hydrocarbons can be fed as fuel directly into the SOFCs. Although, high operating temperatures contributes as fuel flexibility, it reduces SOFC materials long term stability and cause material restrictions. Besides, the high cost of ceramic materials, handling difficulties of the materials can be considered as; chemical compatibilility among contacting contents (anode, cathode, electrolyte, and interconnect material) under operating conditions; matching thermal expansion coefficients of the materials; high electronic and ionic conductivity; and high catalytic activity towards fuel oxidation and oxygen reduction [11].

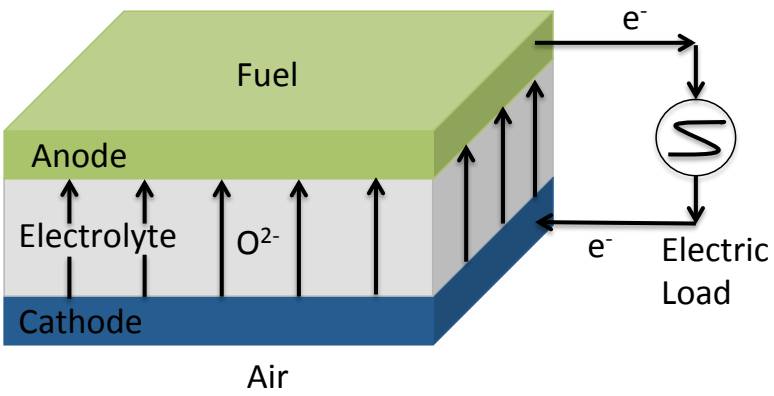


Figure 1.1. Schematic representation of SOFC operation.

The operation scheme for SOFC is given in Figure 1.1. As mentioned in section

1.1 there are three main compartments in a SOFC. For SOFCs these are : i) anode comparment that oxidizes the fuel ii) an electrolyte comparment that conducts O^{2-} ions only iii) cathode compartment that reduces oxygen gas to oxide ions, O^{2-}. Yittria stabilized Zirconia (YSZ), Ni-YSZ and Strontium-doped Lathanum Manganite is used as electrolyte, anode and cathode materials, respectively. YSZ is prefered as electrolyte material due to the high ionic conductivity and low electronic conductivity [12]. Nickel oxide is added to YSZ for anode material to increase the oxidation of fuel and increase the electronic conductivity. Moreover, presence of common material, YSZ, decreases the gap between the thermal expansion coefficients and prevents the cell from cracks at elevated temperatures [13]. Lanthanum strontium manganite (LSM) is used due to the high catalytic activity and high ionic-electronic conductivity. The reduction of oxygen at the cathode occurs via the reaction of 1.1.

$$O_2 + 4e^- \rightarrow 2O^{2-} \tag{1.1}$$

O^{2-} ions produced on cathode side are transported from cathode through electrolyte to electrochemically active sites known as triple phase boundries (TPBs) on the anode side. TPBs are the most dense reaction sites at electrodes where the electrode, electrolyte and the fuel gas come together. On the anode side trasported O^{2-} ions then react with H_2 mostly at these TPBs according to the reaction 1.2.

$$H_2 + \frac{1}{2}O_2^{2-} \rightarrow H_2O + 2e^- \tag{1.2}$$

Following the above reaction, released electrons migrates back to cathode from an external electric circuit, thus generating electric current.

1.3. Materials

Basic operating principles and conditions of SOFC determine the key requirements for each component. All materials must be chemically compatible with each other and have chemical and physical stability towards operation conditions of SOFCs.

Moreover, materials should posses suitable ionic and electronic conductivity according to the compartment they are involved in. The cost of the materials should be low and easy to fabricate although they need be to strong when the high operation temperatures of SOFCs are considered.

1.3.1. Anode

According to basic principles for SOFC anode materials should have high catalytic activity for oxidizing the arriving fuel. Thus, metals can be used as anode material. However, metal must neither be oxidized nor react with other materials under the operating conditions of SOFCs. The anode should be porous enough for the fuel to penetrate into the anode layer until the electrolyte and to promote charge transfer on the TPBs. This is achieved by dispersing metal in the solid electrolyte material to form a cermet which prevents the microstructure from corruption during the operation. The anode must be not only ionicaly but also electronicaly conductive. Doping solid electrolyte with metal contributes to electronic conductivity and compatibility of the materials. Ni-YSZ cermets are employed conventionally in the SOFCs. Yittria stabilized zirconia (YSZ), which is also used as a solid electrolyte material, and Nickel have different thermal expansion coefficents [14]. An anode with pure Nickel directly causes crackings and leakages during the operation.

Ni-YSZ cermets remain as the most common anode material for SOFCs due to their low cost, chemical stability at high temperatures and the close thermal expansion coefficients with the YSZ electrolyte. In addition Ni and YSZ are not reactive over a wide temperature range. Ni-YSZ is obtained by mixing NiO with YSZ with a 1:1 ratio. Nickel is excellent catalyst at $in-situ$ reforming, shifting and cracking of hydrocarbon fuels. But these lead to rapid carbon deposition and coking on the anode surface which basicly deactivates the cell by blocking surface reactions [15].

Ceria based oxides(e.g. Gadalinium doped ceria oxide,GDC) are preferred due to being excellent electrocatalyst for CH_4 and good oxygen ion conductor [16]. The anode showed a close electrochemical performance to Ni-YSZ cermet which are currently the

common anode material used for high temperature SOFCs. Doping Copper(Cu) into ceria based oxides increases resistance towards carbon deposition [17]. Also doping ceria based oxide with Mn reported very good methane oxidation without exess steam [18]. The redox stability and the capacity to operate with low steam hydrocarbon fuels of the metal-oxide-doped anode materials promise to overcome the major limitations of Ni-YSZ cermets, high operating temperature and carbon deposition on the electrode surface [19].

1.3.2. Electrolyte

Solid ceramic electrolytes, such as in SOFCs, enables ions to migrate through the vacancies within the lattice. Ions transfer through this process are called 'Charge carrier ions'. The SOFC electrolytes conduct O^{2-} ions from these vacancies. In addition to ionic conductivity, SOFC electrolyte must have redox stability towards reducing and oxidizing atmospheres. Unlike anode electrode, electrolyte must have low electronic conductivity and non-porous to prevent short circuit in reverse direction and mixing of the fuel with oxidant gas feed, respectively. Electrode material must be unreactive and compatible towards other materials. Moreover, it must have high physical strentgh to endure high operating temperatures with a low cost. The crstytal structure available for this transport is achieved by doping one oxide material into one another. Yittria stabilized zirconia (YSZ) is commonly used as SOFC electrolyte material. Zirconia (ZrO_2) has a cubic fluorite structure above 2370 ^{0}C and Yittria (Y_2O_3) is doped with zirconia (ZrO_2) to stabilize the cubic structure from room temperature to its melting point (2680 ^{0}C) [12, 13]. The optimum doping percentage of yittria is 8 moles percent. At higher dopant ratios, ionic conductivity decreases due to defect ordering, vacancy clustring or electrostatic interactions [20]. The formation of the oxygen vacancies in the fluorite type crsytal lattice is shown in Figure 1.2.

YSZ is highly conductive towards O^{2-} ions and shows high resistance to electrons, but requires operating temperatures above 800 ^{0}C [21]. Thus, other metal oxides are investigated to lower the operating temperatures of SOFCs. Ceria-based electrolytes (gadolinia doped ceria, GDC) have high ability to conduct ions at low temperatures but

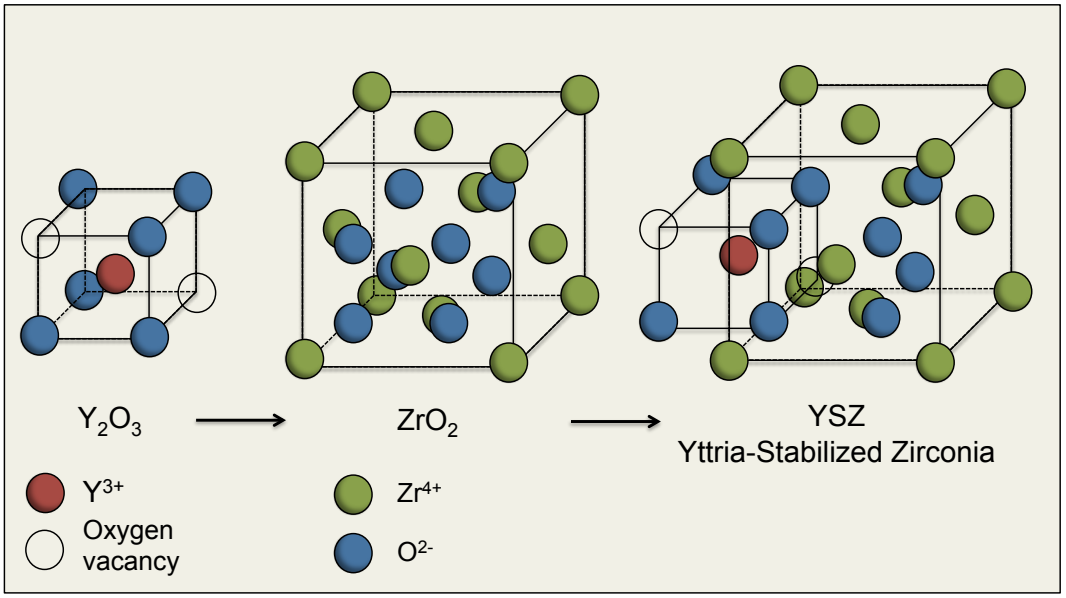


Figure 1.2. Schematic representation of yttria, Y_2O_3, stabilized zirconia, ZrO_2, (YSZ).

GDC causes performance losses because of its mixed ionic-electronic conductivity [22].

1.3.3. Cathode

Cathode material of SOFC must have high catalytic activity for oxygen reduction and high ionic and electronic conductivity like anode material. Cathode also must be porous since there are TPBs in the cathode compartment. Thermal expansion coefficient of the cathode material must be compatible and unreactive towards electrolyte material at high operating temperatures of SOFC.

Materials with perovskite-type structures are commonly preferred due to their good electronic conduction at high temperatures [23]. Strontium-doped lanthanum manganite (LSM) with perovskite type structure is the most commonly used cathode material in current zirconia based SOFCs. LSM satisfies all the requirements for cathode compartment but it reacts with YSZ at higher temperatures and forms lanthanum zirconate (LZO) [24]. Therefore, sintering temperature during the fabrication of the cathode must be below 1300 ^{0}C [25]. Also, stronium-doped lanthanum cobaltite (LSCo), stronium-doped lanthanum ferrite (LSF) and strontium-doped lanthanum cobalt ferrite (LSCF) are the other most widely used cathode materials [26].

Many of the cathode materials are excellent at mixed ionic-electronic conduction at high SOFC operating temperatures and good at oxidation of oxygen. But their reactivity towards YSZ electrolyte and lack of long term stability at high operating temperatures prohibits them involve in zirconia-based SOFCs [27].

1.4. Characterization and Analysis

1.4.1. Electrochemistry

Performance analysis of the SOFCs are evaluated by Electrochemical Impedance Spectroscopy (EIS) and Linear Sweep Voltammetry (LSV). EIS and LSV are applied by a device called potentiostat which is connected to the MEA surfaces on both electrodes with interconnection mashes and cables. Potenstiostat measures the changes in the open circuit voltage (OCV), the current density (J) and the potential (V).

During the operation of a SOFC, losses on the potential occur due to the resistances of the electrodes and electrolyte, physical and chemical prosses taking place on the electrodes [28]. These losses are called voltage losses or overpotentials which affect the open circuit voltage (OCV).

The open circuit voltage is the difference of electrical potential between two electrodes of a cell when there is no external potential or current applied. Reversible cell voltage or Nernst potential (V_{rev}) in a SOFC system can be calculated by diffracting voltage losses from the OCV, according to Equation 1.3.

$$V_{rev} = OCV - \eta_{ohm} - \eta_{act} - \eta_{con} \tag{1.3}$$

where η_{ohm} is the voltage reduction due to ohmic losses, η_{act} is the overpotentials due to activation losses of the electrolytes and η_{con} is the losses of potential caused by gas species concentration changes. OCV can be calculated according to Equation 1.4.

$$OCV = -\Delta G/nF \tag{1.4}$$

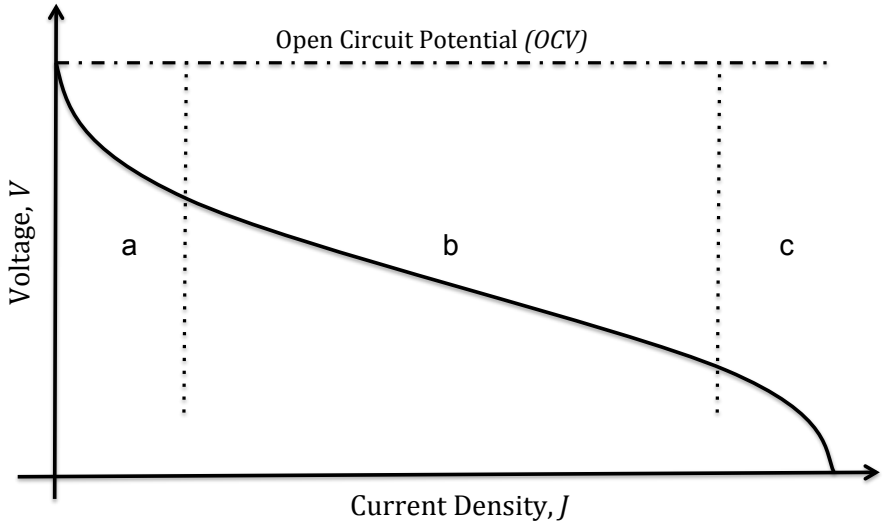


Figure 1.3. Schematic graph of the voltage drop of SOFC as a function of withdrawn current density, a) low current regime, b) medium current regime, and c) high current regime.

where ΔG is the free energy of global oxidation reaction in SOFC when no current flows or no gas transport from one electrode to another. Ohmic losses depending on the resistance of the material and the cell geometry can be obtained from Equation 1.5 where R_{ohm} is the resistance of the MEA [29]. In a real SOFC system resistances of the electrodes are negligable. In addition, using current density (J) instead of current (I) is more convenient due to the mixed ionic-electronic conducting properties of SOFCs.

$$\eta_{ohm} = R_{ohm}.I \tag{1.5}$$

Activation losses at the electrodes, η_{act}, can be calculated from Butler-Volmer equation 1.6.

$$J = J_0[exp(\frac{\alpha_1 nF\eta_{act}}{RT}) - exp(-\frac{-\alpha_2 nF\eta_{act}}{RT})] \tag{1.6}$$

J_0 is the exchange current density, α_1 and α_2 are the transfer coefficients of the forward and the backward reactions, respectively. n is the number of electrons transfered. F is the Faraday constant and η_{act} is the activation loss.

Concentration losses are caused by the concentration change during the mass transport processes of the reactants and products. The concentration difference of the gas species between the reaction zones and the channel flow can be calculated by employing Nernst equation. η_{con} can be calculated from equation 1.7 by employing Nernts potential to the bulk composition at the gas channel and the reaction zones. OCV_{bulk} is the potential difference at the gas channel and OCV_{react} is the potential difference at the reaction zones.

$$\eta_{con} = OCV_{bulk} - OCV_{react} \tag{1.7}$$

Voltage drop of the SOFCs can be identified from Figure 1.3. Withdrawn current density of the SOFCs can be investigated in three parts: low current regime (a), medium current regime (b) and high current regime (c). Voltage vs Current Density plot can be obtained by linear sweep voltammery which is the technique measuring the current at a working electrode while the potential between the working electrode and the reference electrode is swept linearly in time.

The dissociative adsorption of hydrogen, electrochemical processes and charge-transfer reactions on anode surface and TPBs cause the activation overpotentials [30]. The effect of activation overpotentials is responsible for the decay in the low current regime, Figure 1.3 (a). Activation overpotentials are also effective in the medium current regime, Figure 1.3 (b), but activation overpotentials are not the only source of power loss in this regime [31]. The ohmic losses dominate the shape of the polarization curve in medium current regime. The linear decay in the medium current regime caused by the ohmic losses indicates low ionic conductivity of the electrolyte. Losses arised from concentration changes start to affect the polarization curve from the medium current regime and continue to influence the curve until the end of the high current regime, Figure 1.3 (c). Reduction in the concentration leads to a change on the free energies of the involved reactions. In the medium current regime Figure 1.3 (b), the adsorption of hydrogen has a contribution to voltage drop. In the high current regime Figure 1.3 (c), concentration changes due to the surface diffusions and desorptions of

reactants and products lead to voltage losses.

Performance test while operating for such a certain time can also be held by employing choronoamperometry. Another technique applied for the anaylsis of the SOFC. In this technique applied voltage on the working electrode is stepped and generated current is measured over time. This technique is limited for the electrochemical characterization of the MEA but very useful at indicating the differance of the fuel consumption on the anode at different overpotentials.

The SOFCs have both resistive and capacitive properties due to their mixed ionic and electronic conductivity. Charged ions kept inside the cell during the transport from cathode to anode makes the cell function as a capacitor. EIS measures the opposition to the flow of alternating current (AC). Since the SOFCs have both resistive and capacitive characteristics, the opposition to the AC is not purely resistive. A potentiostat is used to apply alternating current, $\Delta j(\omega, t)$, and to receive the opposition as alternating voltage, $\Delta V(\omega, t)$:

$$\Delta j(\omega, t) = V_m.e^{-iwt} \tag{1.8}$$

$$\Delta V(\omega, t) = v_m.e^{-i(wt+\phi)} \tag{1.9}$$

where ω is the angular frequency, t is the time, V_m is the potential, I_m is the current density and ϕ is the phase difference between the potential and the current density. The impedance, Z, is defined as

$$Z(\omega) = \Delta V(\omega, t)/\Delta j(\omega, t) = (V_m/I_m).e^{i\phi} \tag{1.10}$$

$$|Z| = V_m/I_m \tag{1.11}$$

by applying Euler equation

$$e^{i\phi} = \cos\phi + i\sin\phi \tag{1.12}$$

the impedance would be

$$Z(\omega) = Z_{re}(\omega) + Z_{im}(\omega) \tag{1.13}$$

in which

$$Z(\omega) = |Z|.\cos\phi + |Z|.\sin\phi \tag{1.14}$$

$$\tan\phi = Z_{im}(\omega)/Z_{re}(\omega) \tag{1.15}$$

Nyquist representation is commonly used to plot the impedance data. The imaginary part of the impedance is plotted against the real part of the impedance in the nyquist representation as in Figure 1.4.

The $x - axis$ represents the real part,(Z_{real}), of the impadance curve and the $y - axis$ represents the imaginary part, $Z_{im}.Z_{real}$ indicates the resistive processes whereas (Z_{im}) represents the capacitive processes. Resistances of the electrolyte and interconnects are considered as bulk resistance, R_B, at high frequency. The intercept at low frequency of the nyquist plot indicates total resistance,R_T and the difference between R_T and R_B is known as polarization resistance, R_p. All overpotential losses caused by the physical and chemical processes are shown in the R_P by a single arc. Multiple arcs denote multiple processes at different frequencies (ω). Relaxation frequency, ω, is the maximum value at the imaginary part of impedance. In the case of multiple arcs, there exist several relaxation processes with different relaxation frequencies.

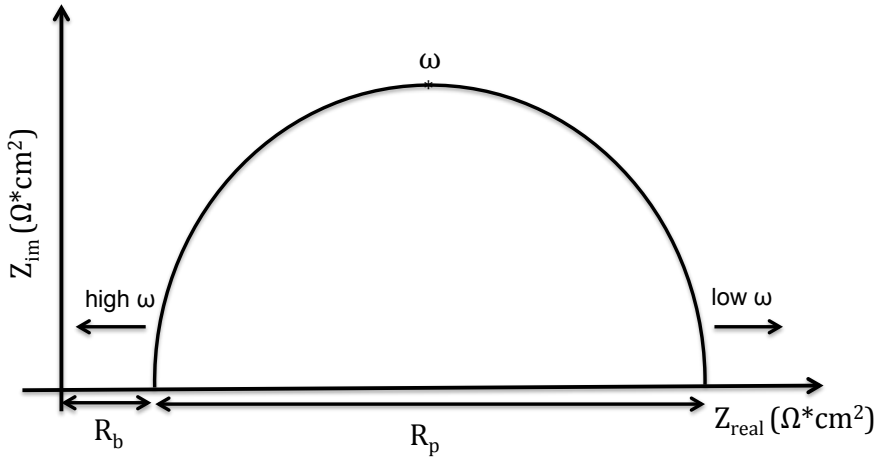


Figure 1.4. Schematic representation of EIS Nyquist plot.

The rate of reactions effects the relaxation frequencies of the processes. Slower reactions take place at low frequencies such as charge-transfer reactions, chemical reactions or transport processes (diffusion, convection) [32].

1.4.2. Analytical Characterization

Elemental composition of the anode and cathode surfaces are observed based on their oxidation states with X-ray photoelectron spectroscopy, (XPS). XPS spectrum is obtained by irriadiating a surface with a beam of X-ray and measuring the kinetic energy of the electrons that escaped from the top 0 to 10 nm of the surface. XPS enables to analyze the surface composition before and after the operation of SOFCs. Degredation of the electrode surfaces due to the electrochemical processes during the operation of SOFC can be investigated. Moreover, several irreversable poisoning side reactions occuring due to the fuel diversity can also be observed.

Crystal structure of the electrode and electrolyte materials can be investigated by X-ray diffraction (XRD). An X-ray beam is diffracted by the crystalline atoms into many specific directions. A crystallographer produces a three dimensional picture of the electron density of the crystalline from the diffrected beams. From the density of electrons the mean position of the atoms in the crystal and their chemical bonds can be determined.

Raman spectroscopy is used to understand the vibrational modes of the materials. Raman spectroscopy measures the scattering of light caused by the vibration of molecules unlike Infrared spectroscopy (IR) in which absorption of ligth is measured. The inelastic scattering of light is collected with a lens and detected by a monochromator.

In addition, Image of the surface and the topography of the surface can be analyzed by scanning electron microscopy (SEM) and atomic force microscopy (AFM), respectively.

1.5. Fuel Types

Fuel in SOFCs is for the oxidation of O^{2-} ions transported through the porous electrolyte. Low partial pressure of oxygen at the anode side of the MEA creates the driving force for the transport of the O^{2-} ions [10]. Hence, molecules in the content of the fuel must have the ability to oxidize oxygen ions. The high operating temperature of SOFCs enables to utilize not only hydrogen but also different types of hydrocarbon fuel sources as oxidizing agent for oxygen ions [33].

hydrogen gas, H_2, is the ideal fuel for the fuel cells due to its high reactivity and zero emission property. But fuel production as hydrogen and its storage are not widely spread, yet. Natural gas, methanol, gasoline and coal are commonly used sources for hydrogen production. The production of hydrogen includes a series of processes such as desulfurization, reforming, water-gas shift reaction(Equation 1.16) and carbonmonoxide (CO) removal. For the fuel cells using both H_2 and CO such as solid oxide fuel cells(SOFCs) and molten carbonate fuel cells (MCFCs), CO removal step can be skipped.

$$CO + H_2O \rightleftharpoons CO_2 + H_2 \tag{1.16}$$

Hydrocarbons can be utilized in the SOFCs and MCFCs. After reforming processes are applied to higher hydrocarbons, a gas mixture composed of CO, H_2 and CH_4 is

synthesized. CO and H_2 are used as fuel already but CH_4 does not used as a fuel directly since the reaction of CH_4 at the electrode as a fuel is much more slower than the internal reforming into CO and H_2 (Equation 1.17) [34].

$$CH_4 + H_2O \rightleftharpoons CO + 3H_2 \tag{1.17}$$

There are several sources for CO, H_2 and hydrocarbons such as fossil fuels. With the help of the reforming processes fossil fuel sources are converted into syngas mixtures. The major one of these sources is coal with the largest reserves existing. Syngas produced by the gasification of coal includes the necessary fuel content for SOFCs, thus can be used as an efficient fuel source. The gasification processes of coal includes purification and reforming steps. Purification of the coal syngas is applied directly after the gasification of coal at 900^0C in two steps. First step is to get rid of the larger particles such as tar by a cyclone filter and second step is to eliminate small sized impurities such as phosphor, sulfide, etc.. by zeolites or mesoporous silicates [35]. Reforming of methane which is obtained by coal gasification and purification could be carried out internally or externally. It was reported that internal reforming is more efficient than external reforming in SOFC systems [34].

1.6. Fuel Conditioning and Monitoring

Gasification of coal is a thermochemical process that generates a fuel rich syngas. Processes involved in the gasification are pyrolysis, steam reforming and purification, respectively. Pyrolysis, thermochemical decomposition, generates a solid residue richer in carbon residue and a syngas including CO, CO_2, H_2, hydrocarbons, tars and impurities [35]. Syngas produced is treated with steam at elevated temperatures to reform hydrocarbons into CO, H_2 (Equation 1.18). High temperature and low pressure conditions shift the equilibrium of steam reforming reaction 1.18 to H_2 production according to Le'Chatelier principle since steam reforming of hydrocarbons is endothermic [34].

$$C_nH_m + nH_2O \rightleftharpoons nCO + (n + m/2)H_2 \tag{1.18}$$

Another reaction taking place in the gasification process is the water-gas shift reaction (Equation 1.16), which produces CO_2 and H_2 as products [36]. Unlike the endothermic reaction of steam reforming, water-gas shift reaction is exothermic. The reaction conditions of high temperature and low pressure favors in the reverse reaction and prevents all CO turn into CO_2 according to the Le'chatelier principle [37]. This leads to the necessity of CO removal in order to use the reformed syngas in low temperature fuel cells. SOFCs are able to utilize CO also as fuel but other impurities in the syngas still have to be filtrated to prevent the cell from coking or poisoning. Tar content in the syngas can be removed by physical filtration. But to the impurities in the content of the syngas other than tar chemical filtration should be applied. Be, Cr, K, Na, and V exist in the syngas in trace amounts [38]. Altough SOFCs are affected by the existing gas species of Hg, Si and Zn, their reactions with the electrodes are reversable and can be purged N_2 [39]. Reactions of Cl, Sb, As, and P are irreversible and they severly poison the MEA and cause voltage degradation [38]. Silicon zeolites can be used as chemical filtration due to its 0.56 nm pore size which only allows the fuel gasses of CH_4, H_2O, H_2, CO, and CO_2 with pore sizes of 0.40 nm and smaller [35].

Monitoring of these fuel gas species are achieved by Mid-IR absorption spectroscopy [40]. Different molecules absorp different wavelengths of light. Fuel gases of CH_4, CO, CO_2, and H_2O have absorption spectrum between 1.5 and 5 μm which is the middle of the infrared spectrum. IR radiation is absorbed into the vibrational modes of the molecules in gas phase. The absorption of IR light decreases the intensity of the transmitted light through the fuel gas molecules. The ratio of the transmitted intensity, I, to the incident intensity, I_0, is called transmittance,T:

$$T = \frac{I}{I_0} \tag{1.19}$$

Absorbance, A, of the sample at a given wavenumber can be defined as:

$$A = log\frac{I_0}{I} \qquad or \qquad A = -logT \tag{1.20}$$

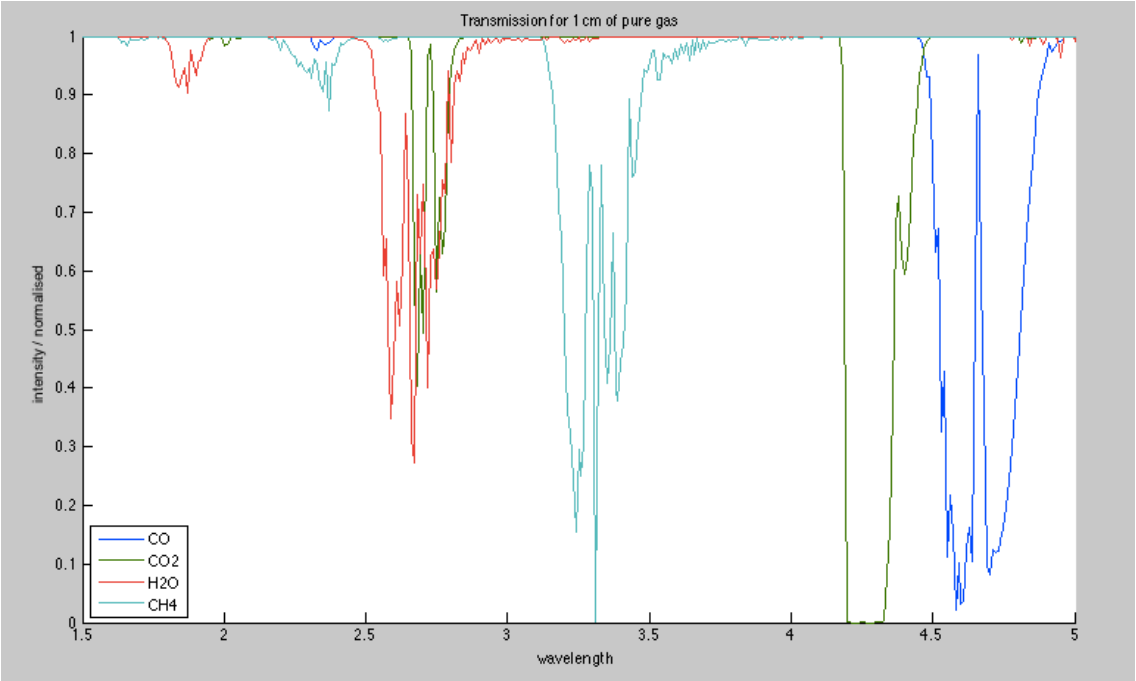


Figure 1.5. Calculated transmission spectra of involved gas species.

It is found that intensity tranmitted is relevant with path length, l and molar concentration, C, of the sample in accord with the Beer-Lambert's law:

$$A = \varepsilon \ell C \tag{1.21}$$

Absorptivity or molar absorption coefficient, ε, depends on the frequency of the incident radiation and is greatest where the absorption is most intense. Dimensions of the absortivity is 1/(concentration x length).

Transmitted radiation, decrease in the intensity of the incident light, is detected by a photodetector composed of PbSe. Infrared radiations are derived from five different light emitting diodes (LEDs) radiating at different wavelengths in the mid-IR spectrum. Wavelengths of the LEDs are selected according to the absorptivities of the involved fuel gas molecules. As shown in Figure 1.5 absorptivities calculated from HITRAN database is between 1.5 and 5 μm [41]. Peaks indicate the intervals where the absorptions are greatest for each gas molecule. From this calculation of absorptivities 5 diodes with 1900, 2050, 2350, 4300 and 4600 nm central wavelengths are selected. At

1900 nm absorption is maximum for H_2O, at 2350 nm absorption is maximum for CH_4, at 4300 nm it is maximum for CO_2 and at 4600 nm absorption is maximum for CO but any diode at a fixed wavelength does not measure absorption of a single gas [42]. As it is in the 2350 nm wavelegth. the absorption is most intense for CH_4 but both H_2O and CO absorbs light in small amounts. The existance of the 2050 nm diode is for this reason. None of the gas molecules have an absorption peak at 2050 but it is expected for CO_2 and CH_4 have aborptions relatively. Due to this mixed aborption amounts, every LED is operated for each gas (CH_4, H_2O, H_2, CO and CO_2) and absorption values are analyzed for the calibration of the system. Since the H_2 molecule is very small and the absorption is insignificant. Concentration of H_2 is calculated by diffracting the sum of concentrations of other gases (CH_4, H_2O, CO, and CO_2) from the total concentration. Thus, mid-IR spectrum, which is the expected absorption spectrum for the involved fuel gases, is swept over a range of wavelengths from 1.5 μm to 5 μm.

1.7. Scope of the Thesis

The aim of the study is to design and develop SOFC operating with syngas and coal gasification integrated system and anaylze the effects of fuel concentration on the SOFCs' performance electrochemically and analitically.

Performance tests consisting of linear sweep voltammetry and EIS are used for the electrochemical characterization. $In-situ$ monitoring of chronoamperometry and mid-IR absorption spectroscopy measurements are observed for analytical characterization. Linear sweep voltammetry, electrochemical impedance spectroscopy and chronoamperometry measurements are completed by using a potentiostat. Test rig for electrochemical and analytical analysis, test stack separated by bipolar plates and fuel monitoring system is specially designed for electrochemical and analytical analysis.

Open circuit voltage and maximum power values are obtained from linear sweep voltammetry experiments. Open circuit voltage shows the minimum amount of fuel concentration for the system to reach the equilibrium. Maximum power values indicate the anodic overpotential where the SOFC has the highest efficiency.

Bulk resistance and polarization resistance values are obtained from electrochemical impedance spectroscopy. Bulk resistance values indicate the ohmic drop and polarization resistance values show the concentration polarization. The concentration polarization is expected to decrease with the increase of the fuel concentration.

Simultaneous monitoring of $in - situ$ SOFC exhaust analysis indicates the fuel conversion efficiency. Thus, supplied fuel concentration and collected current from the SOFC system is evaluated quantitatively to calculate the fuel conversion efficiency. These evaluations show that the fuel conversion efficiency values are in the range of 11 to 19 %.

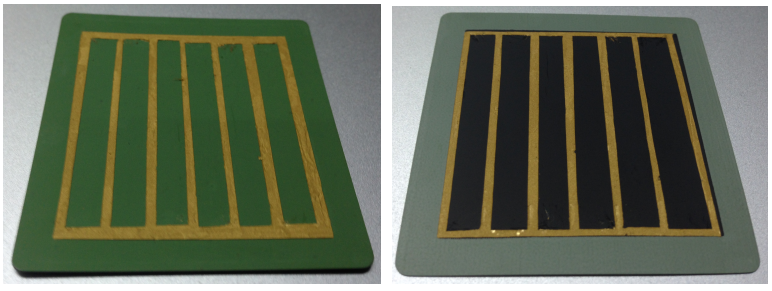
2. Experimental

2.1. Experimental setup

The MEA used for experiments are composed of Ni-YSZ, YSZ and LSM in the anode, electrolyte, and cathode, respectively. The MEA is a square shaped planar SOFC with the dimensions of 50x50 mm and 25 cm^2 surface area. The thickness of the MEA is 0,4 mm. Planar SOFC is chosen for the experiments due to the stack configuration of the SOFC test rig. Shape and dimensions are determined according to not only the stack configuration of the test rig but also efficiency. Surface area of 25 cm^2 is large enough to produce necessary power. MEAs with larger surface areas increase the possibility of cracking during the operation and MEAs with smaller surface area would not be able to produce the power satisfying the system unless the MEA number is increased with a multiple stack configuration.

2.1.1. Preperation of The MEA and SOFC Stack Design

The MEA surface is covered with gold paste in order to increase the rate of current collection from the surface. The tandem shape of the gold paste coverage can be seen from Figure 2.1.



(a) Anode (b) Cathode

Figure 2.1. Gold paste application on the surface of the membranes.

Gold mesh of 5mm x 1mm is prepared to place on the electrodes over the gold paste perpendicular to the tandem lines (Figure 2.2). The gold meshes are the only layer in between MEA and bipolar ceramic plates of the SOFC stack (Figure 2.3). These meshes are connected to the potenstiotat with gold wires in order to apply electrochemical tests. The MEA is placed in between bipolar ceramic plates according to their gas flow channels. Glass wool and natural muscovite is used as gasket to prevent gas leakage around the MEA. The gas channels are sculpted inside the bipolar ceramic plates but the gap caused by the thickness of the MEA must be filled to avoid both gas leak and interference of anode and cathode gases. Serpentine gas flow channels on the bipolar ceramic plates can be seen from Figure 2.4.



Figure 2.2. Gold mesh at the bottom of cathode layer.

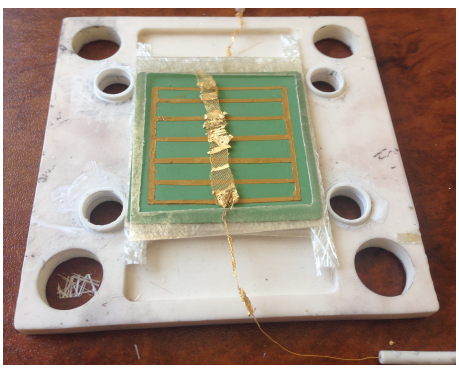


Figure 2.3. Gold mesh on the top of anode layer.

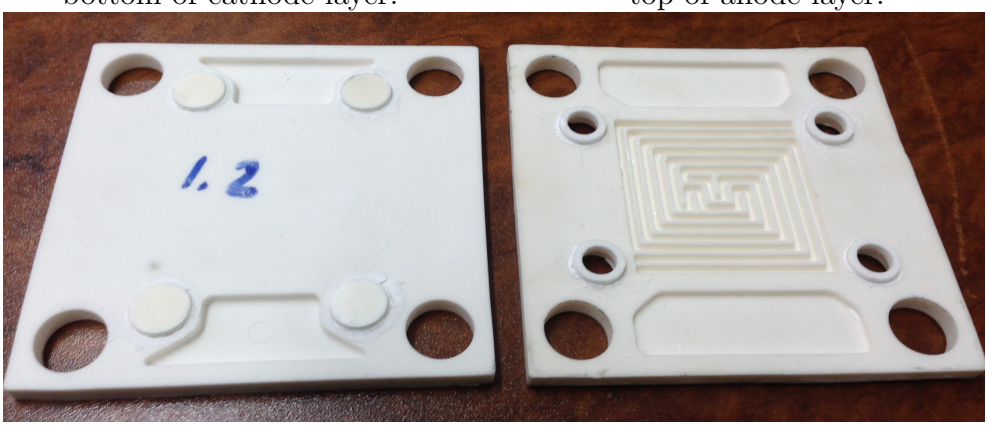
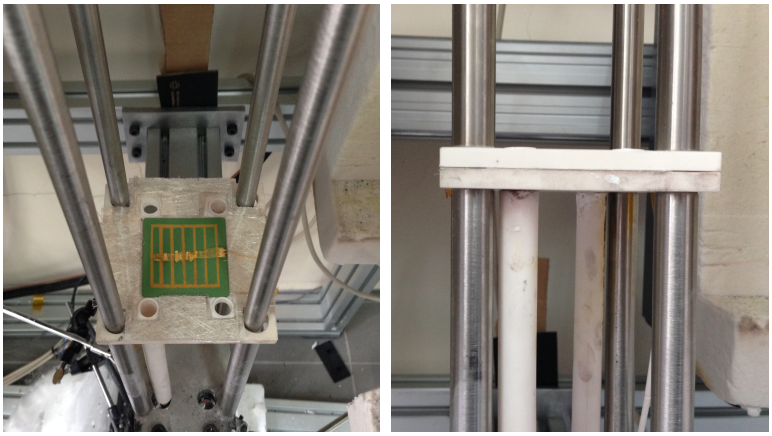


Figure 2.4. Bipolar seperating plates.



(a) Top View (b) Side View

Figure 2.5. SOFC stack in the SOFC test rig.

2.1.2. SOFC Test Rig

Stack configuration and design of polar plates of the stack can be seen from Figure 2.4. The plates are made of Aluminum oxide material, which is inactive for mentioned fuel gases, to resist the high operation temperatures of SOFCs. Gas inlet and outlet of the inner cycle of the stacks are held through the gas pipe holes on the plates. The serpentine gas channels on the plate is designed to increase the retention time of the surface reactions of the fuel gas on the membrane (Figure 2.4).

Polar plates are attached each other with a special gasket placed on the edges of the gas channel holes and pasted to each other with a special ceramic paste, Aremco. In between the plates a sealing frame to prevent fuel gas leakage is placed. First layer placed on the polar plate to avoid gas leakage is composed of muscovite, then, glass wool layer is placed over it. Four muscovite and one glass wool layer is placed Type of the muscovite and glass wool used in this study is determined according to their resistance to high operating temperatures of SOFCs. MEA is placed between bipolar plates and surrounded by muscovite and glass wool as insulation material.

SOFC stack is placed on the SOFC test rig. Test rig consists of a high temperature oven whose sides can be separated from each other, four bars to place the SOFC, four gas channel pipes composed of alumina (Al_2O_3) material for anode and cathode fuels



Figure 2.6. Experimental setup of SOFC Test Rig.

and exhausts, mass flow controllers, a potentiostat and fuel monitoring system. As the system operates gas fuels and exhaust gases flow through steinless steel pipes which connects all the comportments of the integrated system (Figure 2.6). Steinless steel pipes are covered with heating elements to prevent condensation of circulating gases. Also, bars that hold the SOFC stack is composed of steinless stell. During the operation of the SOFC, holding bars of the SOFC stack must not expand and cause gas leakage.

At the bottom entrance the SOFC oven steinless steel pipes are connected to aluminum oxide pipes with a special connector. Fuel gases are transported into the oven with alumium oxide pipes which are attached to the polar plates from the bottom part. Steinless steel pipes must not be connected to the bipolar plates directly since their thermal expansion coefficients are highly different.

2.1.3. Fuel Monitoring System

Device assembled for concentration monitoring of fuel gases by absorption spectroscopy consists of 5 mid-IR light emitting diodes(LEDs) with 1950, 2050, 2350, 4200 and 4600 nm central wavelengths and a PbSe amplified photoconductive detector with

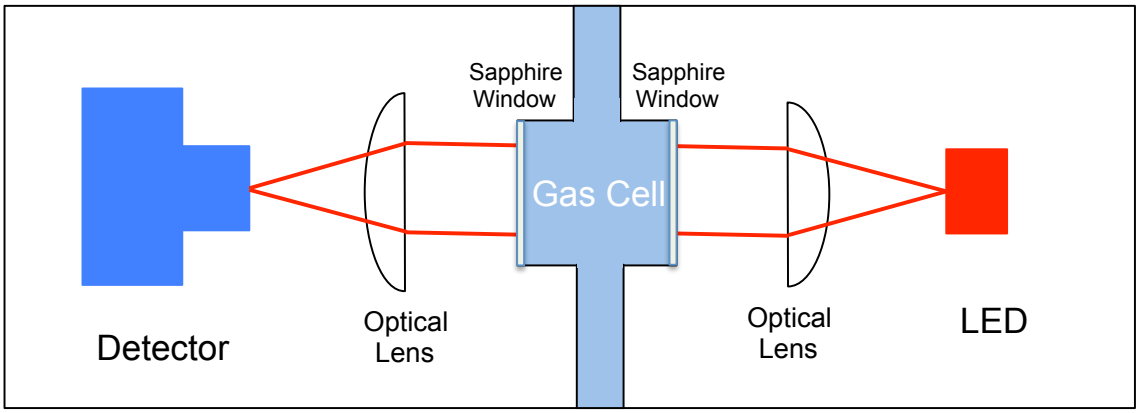


Figure 2.7. Schematic representation of optical allignment of the fuel monitoring system.

a detection range of 1 to 5 μm (for 50 Ω load). MID-IR spectra from 1500 nm to 5000 nm is the detection spectrum of the involved fuel gases. Central wavelengths of 5 mid-IR LEds are determined according to the absoprtivity of the fuel gases on the specified absorption range. Absorptivities of the fuel gas molecules are calculated from HITRAN database. Absorptivities of CH_4, CO, CO_2, and H_2O gases are shown in Figure 1.5.

Sapphire windows are used for the monitoring window on the gas cell. Except sapphire glass no material permit the transmission of light above 4000 nm efficiently. Lenses are alligned to collimate the beam of emitted light from the LEDs by collimating and focusing. Calcium fluoride lenses are used to allow transmission in mid-IR. Gas cell components are also consist of steinless steel. A schematic of the experimental gas analysing system can be seen from Figure 2.8.

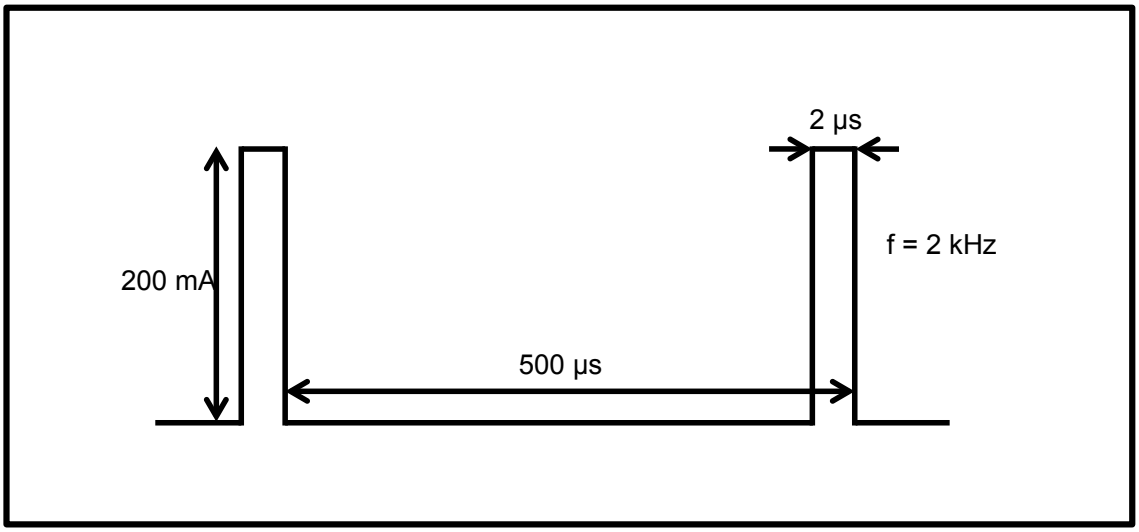


Figure 2.8. Schematic representation of applied square signal to drive the LEDs.

A square signal with 2 kHz frequency and 0.4 percent duty cycle is used to drive the Thorlabs LEDs, Figure 2.7. But the magnitude of the driving signals for the LEDs differs according to their optical power outputs. LEDs with lower central wavelentghts 1900 nm, 2050 nm and 2350 nm have optical power above 0.8 mW. Optical power range between 0.8 and 1.1 mW is enough for the LEDs to be driven by a signal of 200 mA. Whereas a current of 1 A is used to drive LEDs with higher central wavelengths, 4300 nm and 4600 nm, since their optical power is below 6 μW.

The signals emitted from the LEDs are fed into a PbSe Thorlabs PDA20H photodetector. Difference in the intensity of light is detected by the photodetector in the +/- 10 V range. The signal detected by the photodetector is delivered to a laptop with Picoscope digital osciloscope via usb connection. The difference of the signal obtained from the detector and delivered by the oscilloscope indicates the total transmission change over the selected wavelengths not only the detection for the specified gas. Moreover, the transmission at different wavelengths cannot be separated at the detector so every detection at different wavelengths should be calculated accordingly. A Thorlabs CR1-Z7E series rotating stage is employed to switch between the LEDs with different central wavelenghts. The prototype gas analyzer can be seen from Figure 2.9.

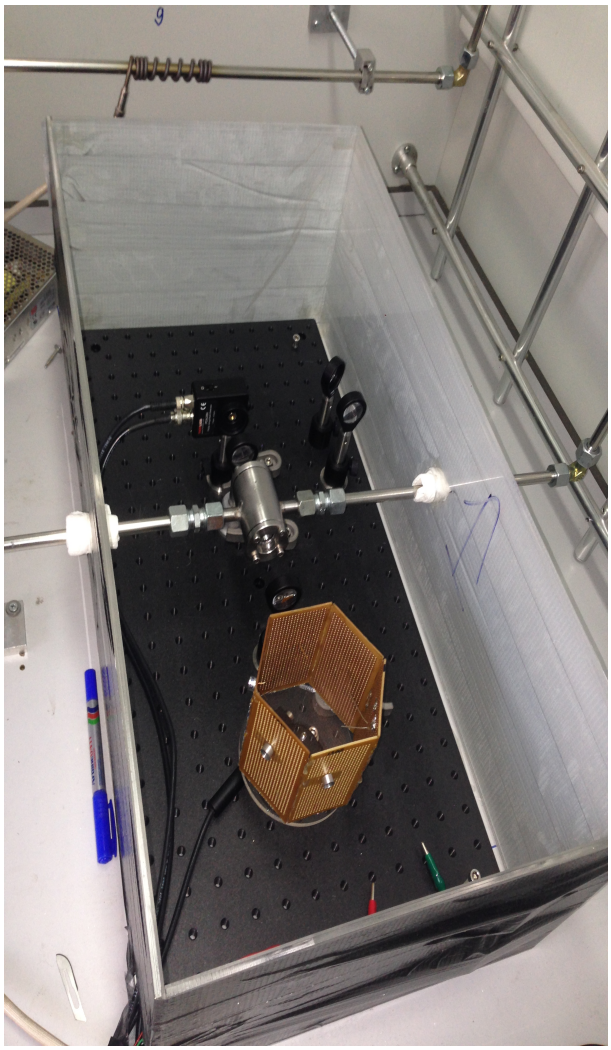


Figure 2.9. Picture of fuel monitoring system.

2.2. Characterization

High operating temperatures of SOFC is achieved by a stepwise heating procedure in order to prevent cracking of the MEA. The oven of the SOFC is heated with 0.5 ^{0}C/min until 400 ^{0}C and 1 ^{0}C/min. This process can be seen from Figure 2.10. Then the temperature controller stabilizes the temperature at 800 ^{0}C for the experiments. During the heating process anode side of the MEA is fed with H_2 and N_2 gases in order to condition the SOFC. Total amount of fuel feed for heating process is 200 sccm, 10 sccm H_2 and 190 sccm N_2.

SOFC is stabilized and conditioned for 20 hours at 800^{0}C of heating process. Then consequently total fuel feed is adjusted to 400 sccm through the remotely controlled mass flow controllers. Open circuit voltage of about -1.0 V indicates the SOFC is ready to operate. EIS experiments with different anodic overpotentials and linear sweep voltammery experiments for different fuel concentrations are applied as the electrochemical analysis. Chronoamperometry and Mid-IR absorption spectroscopy experiments for different CH_4 fuel concentrations are applied as $in-situ$ SOFC exhaust analysis.The SOFC oven is held at 800 ^{0}C until the end of the experiments and cooled to room temperature with a cooling rate of 1 ^{0}C/min for the post mortem analyses. All the electrochemical measurements are applied by a GAMRY REF3000 series potentiostat.

2.2.1. Electrochemical Characterization

Open circuit voltage is monitored through the heating process in order to check whether the cell is stable or not. OCV at 800 ^{0}C of around -1.0 V when SOFC is fed with 400 sccm fuel on the anode and 400 sccm on the cathode shows that the SOFC is suitable for the experiments.

A sequance of nine electrochemical analyses are applied for each gas concentration. The sequence consists of four EIS and five LSV experiments. EIS experiments are applied for OCV, -100 mV, -200 mV and -300 mV anodic overpotentials in order

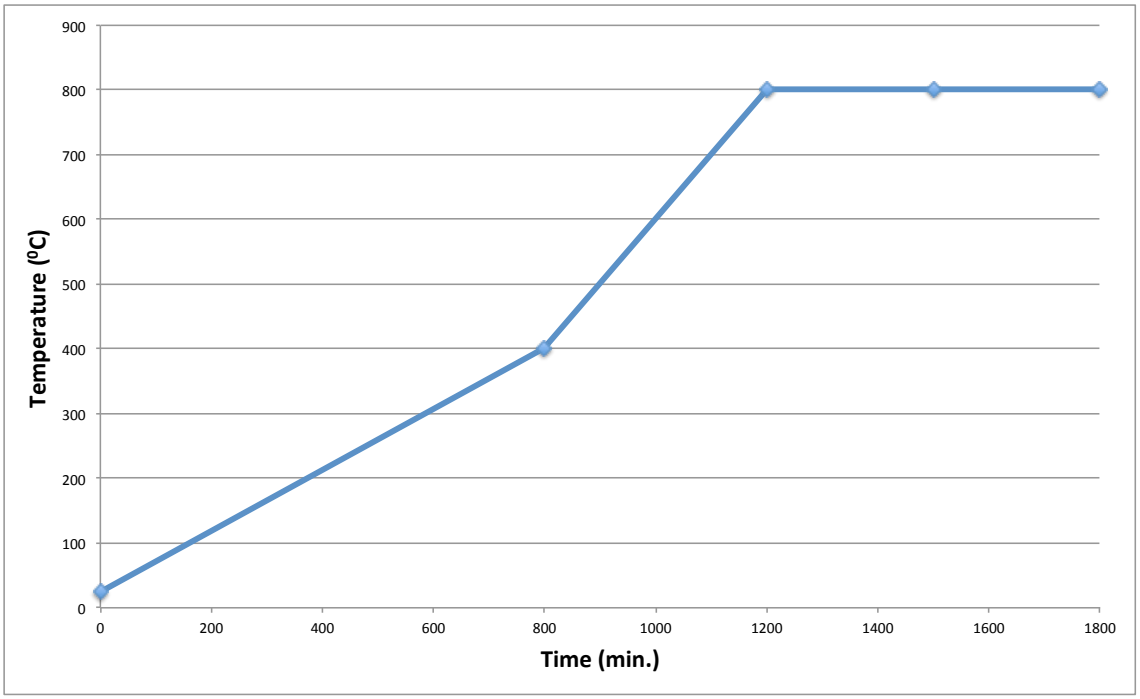


Figure 2.10. Heating program for SOFC operation.

to analyze the limiting steps of the MEA. LSV experiments are applied at the beginning, at the end and in between the EIS experiments to observe the performance of the MEA after and before each EIS experiment. LSV experiments for H_2 fuel is held at a potential range of -1.0 V to 0 V and for CH_4 fuel between -1.1 V and 0 V. The range of the LSV experiments are determined according to the open circuit voltages.

The electrochemical characterization experiments are repeated for different fuel contents of 400 sccm feed. Content of the fuel consist of 100 sccm, 200 sccm, 300 sccm H_2, and 50 sccm, 100 sccm CH_4. N_2 is used as diluent gas in the fuel content and all experimented fuel concentrations of H_2 and CH_4 are complemented to 400 sccm with N_2.

2.2.2. $In-situ$ SOFC Exhaust Analysis

The $in-situ$ exhaust analysis are held for CH_4 concentration measurements but can not be done for hydrogen concentration measurements since hydrogen molecules are too small to detect with absorption spectroscopy. Fuel monitoring system is calibrated

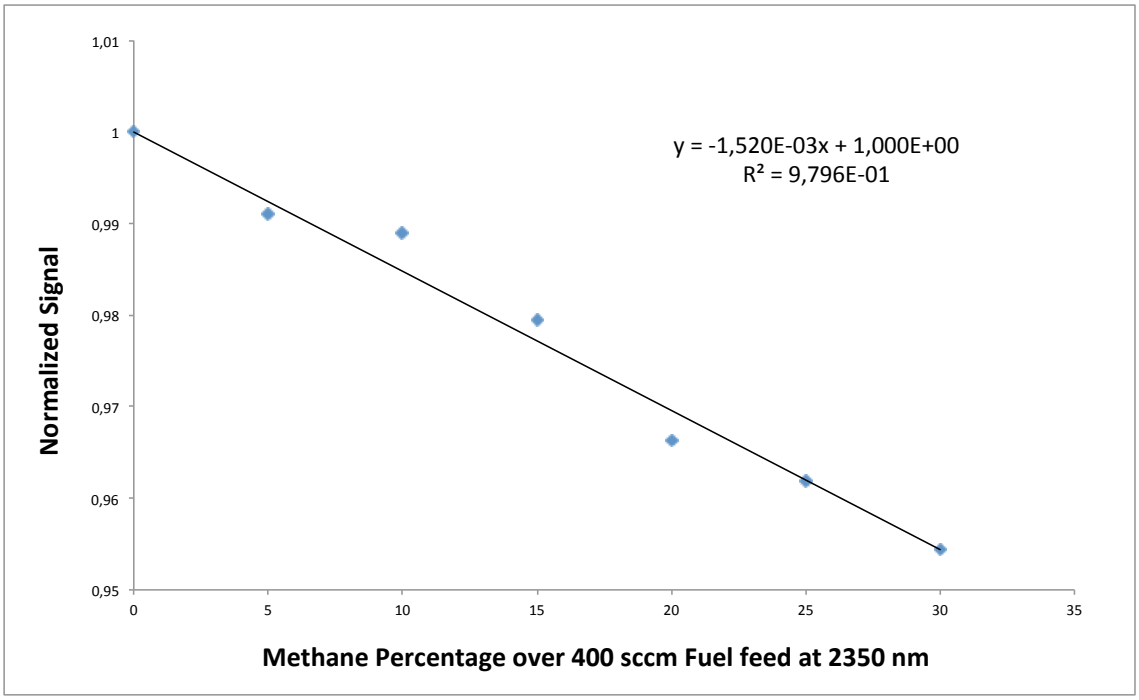


Figure 2.11. Calibration curve for CH_4 with LED2350.

for the CH_4 measuremts of the anode exhaust before the SOFC integrated system is conditioned for the experiments. Steinless stell pipes are heated for the calibration experiments. Absorption line of CH_4 is obtained from the absorption signals of zero methane concentration to 120 sccm CH_4 concentration with 20 sccm concentration increments at 2350 nm. The absorption line is normalized against time. Absorption line of CH_4 at 2350 nm can be seen from Figure 2.11.

Chronoamperometry method is applied to SOFC at 100 mV and 500 mV overpotentials with 50 sccm and 100 sccm CH_4 fuel in order to observe the $in-situ$ reduction of CH_4 concentration when the applied potential is increased on the SOFC. Signals from the photodetector are recorded during the chronoamperometry experiments. Recorded signals are plotted and used to calculate transmittance of light. Then the concentration ratios are calculated via the Beer Lambert's law. The concentration ratios and the current collected from the MEA is plotted in order to determine the reduction trend of different CH_4 concentrations at different anodic overpotentials.

Fuel conversion efficiencies can also be calculated from these concentration per-

centages. The ratio between supplied electronic charge and electronic charge collected from the SOFC system indicates the fuel conversion efficiency. Supplied electronic charge can be calcualted through the ideal gas law and the electronic charge collected from the SOFC system can be calculated from Coulomb's law.

3. RESULTS

Performance and Impedance analysis of SOFC are completed by Linear Sweep Voltammetry and EIS. Linear Sweep Voltammerty enables us to obtain potential and power curves of the SOFC from which the open circuit voltage, maximum power of the MEA and the necessary anodic overpotential to reach that maximum power can be determined. EIS indicates the resistive and capacitive properties of the MEA. Presented EIS plots are consist of real and imaginary parts of the impedance. Thus, bulk resistances, the polarization and total resistances can be observed and limiting steps of the MEA can be addressed by using these analysis.

For the $in-situ$ exhaust analysis, the SOFC is operated with stepping potential in certain time intervals for different fuel concentrations. The absorption signals obtained from mid-IR monitoring system at 2350 nm during this experiment are plotted against time and coupled with collected current.

3.1. Electrochemical Performance

Open circuit voltage of SOFC can be determined from the intercept of y axis in the potential curve. Maximum power and the anodic overpotential necessary for the production of the maximum power can be seen from coupled plot of the potential and power curves. Potential and Power curves of different fuel concentrations are presented in Figures 3.1 and 3.2 for H_2 and CH_4 fuel, respectively. The performance results of SOFC experiment with 100 sccm, 200 sccm and 300 sccm H_2 fuel can be seen from Figure 3.1.

The open circuit voltage of 100 sccm hydrogen is 0.89 V but the OCV of 200 and 300 sccm H_2 fuel feed is higher with 0.96 V and 0.97 V (Figure 3.1). Higher OCV values are expected with increasing H_2 concentrations. So, difference between 100 and 200 sccm H_2 fuel feeds are releated with the expectations but the close OCV values of 200 and 300 sccm H_2 fuel feeds should be inspected.

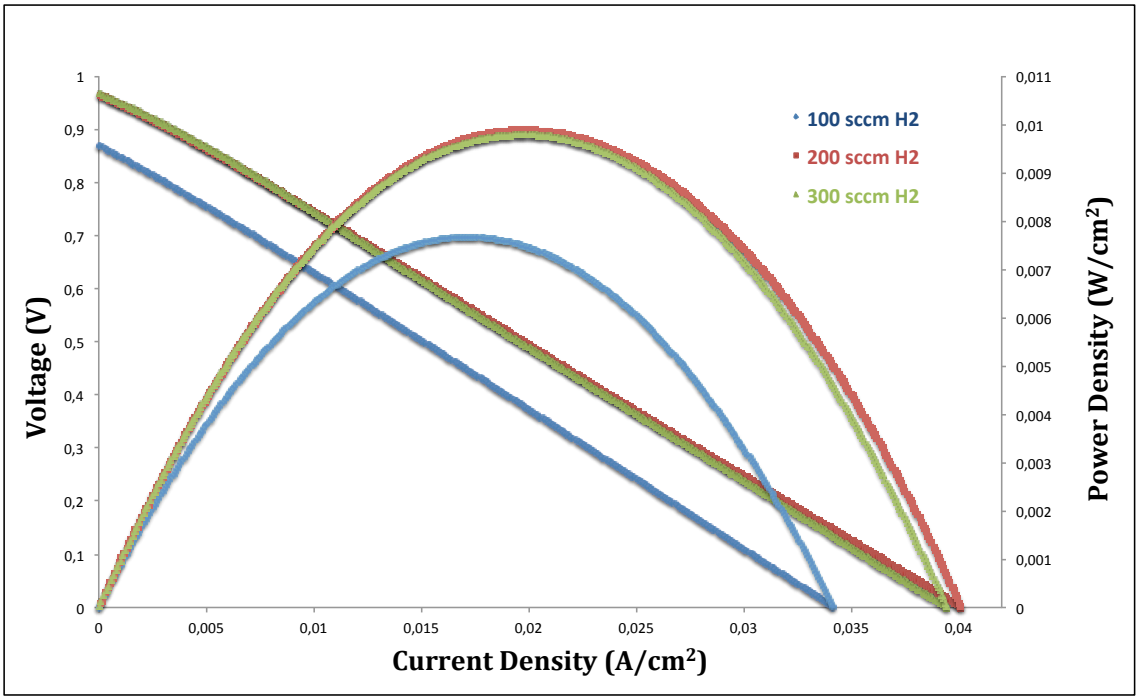


Figure 3.1. Performance curves of SOFC running with H_2 flowing at the rate of 100 sccm (blue), 200 sccm (red), and 300 sccm (green).

Maximum power for different fuel concentrations can be determined from the peak of the power curve. Maximum powers of different hyrogen fuel concentrations are 0.00766, 0.00988 and 0.00978 W/cm^2 for 100 sccm, 200 sccm and 300 sccm feed, respectively. The anodic overpotential necessary for the maximum power production is the potential difference between the OCV and the potential of the current density at the maximum power peak. Anodic overpotentials for the maximum power of the 100 sccm, 200 sccm and 300 sccm H_2 fuel feeds are 0.409 V, 0.455 and 0.473 V, respectively. Again the increase of the maximum power with increasing fuel feed is consistent with previous studies.

The performance results of SOFC experiment with 200 sccm hydrogen gas, 50 sccm and 100 sccm Methane gas fuels can be seen from Figure 3.2. The open circuit voltages of 200 sccm hydrogen, 50 sccm and 100 sccm Methane fuel feed are 0.96 V, 0.94 V and 1.03 V, respectively (Figure 3.2). Higher OCV values are expected with increasing fuel concentrations. CH_4 concentrations are lower at volume against H_2 but the amount of reactive ion content towards Nİ-YSZ anode surface of CH_4 concentrations

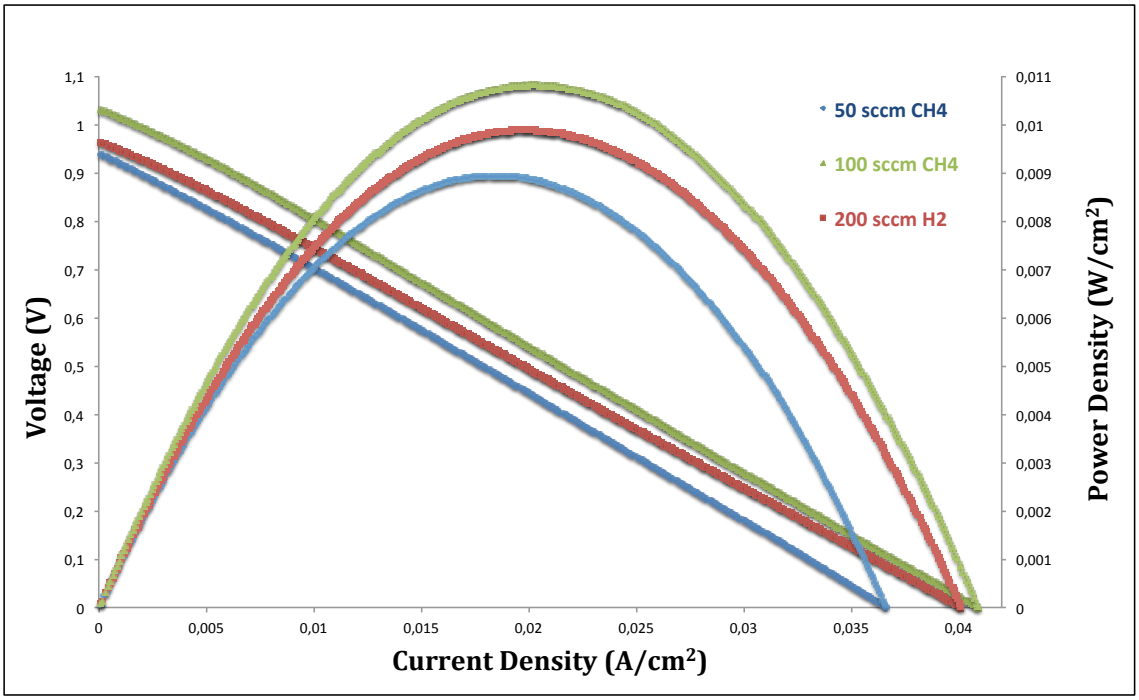


Figure 3.2. Performance curves of SOFC running with H_2 flowing at the rate of 200 sccm (red) and CH_4 flowing at the rate of 50 sccm (blue), and 100 sccm (green).

are equal or higher.

Maximum power for different fuel concentrations can be determined from the peak point of the power curve. Maximum powers of different fuel concentrations are 0.00988, 0.008939 and 0.010815 W/cm^2 for 200 sccm H_2, 50 and 100 sccm CH_4 fuel feed, respectively. The anodic overpotential necessary for the maximum power production is the potential difference between the OCV and the potential of the current density at the maximum power peak. Anodic overpotentials of the maximum power values of the 200 sccm H_2, 50 and 100 sccm CH_4 fuel feeds are 0.455 V, 0.449 V and 0.501 V, respectively. Again the increase of the maximum power with increasing fuel feed is consistent with previous studies.

The open circuit voltage is related to the Gibbs free energy of the reactions taking place (Equation 1.4). The increase of the OCV from 100 sccm to 200 sccm H_2 fuel feed indicates that the reaction is not reached to the equlibrium yet. But the close OCV values of 200 sccm and 300 sccm H_2 fuel feed indicates the system has reached

Table 3.1. Open circuit voltage values (V) for different fuel concentrations.

	100 H_2	200 H_2	300 H_2	50 CH_4	100 CH_4
OCV (V)	0.869	0.963	0.967	0.939	1.03

equilibrium when the system is fed with 200 sccm H_2. Thus, the OCV values of 200 and 300 sccm H_2 fuel feeds are close to each other. One mole of H_2 is oxidized by one mole of oxide ion whereas one mole of CH_4 is oxidized by four moles of oxide ion. So four moles of H_2 is equivalent to one mole of CH_4. Then, 200 sccm H_2 fuel concentration and 50 sccm fuel concentration have the same oxidizing capacity towards oxide ions. But according to OCV values presented in Table 3.1, OCV value of 200 sccm H_2 fuel feed is higher than the OCV value of 50 sccm CH_4 fuel feed. Methane is oxidized to CO and CO_2 where hydrogen is oxidized to water only. Methane could deposit on the MEA where hydrogen does not. Moreover, CH_4 could undergo many more internal reforming reactions due to the presence of water vapour at elevated operation conditions of SOFC. Thus, H_2 is a much better fuel than CH_4 for SOFCs.

The OCV value of 100 scccm CH_4 fuel feed is higher than the OCV value of 50 sccm CH_4 where the OCV values of 300 sccm H_2 fuel feed is not higher than the OCV value of 200 sccm H_2 fuel feed. This is also because of the side reactions taking place when the MEA is operated with CH_4. The anode reactions at MEA might reach to equilibrium with 200 sccm H_2 fuel feed but it is possible that it does not reach to equilibrium with 50 sccm CH_4 fuel feed which has the equivalent reaction capacity towards Ni-YSZ anode surface with 200 sccm H_2 fuel feed.

The maximum power values are presented in Table 3.2. The maximum power of 200 sccm H_2 fuel feed is higher than the maximum power of 100 sccm H_2 fuel feed. This is due to the increased reaction rates with the Ni-YSZ anode surface of the MEA. But the maximum power values does not increase when the system is fed with 300 sccm H_2 fuel. This indicates that the system is saturated above 200 sccm H_2 fuel feed.

Table 3.2. Maximum power values (W/cm^2) for different fuel concentrations.

	100 H_2	200 H_2	300 H_2	50 CH_4	100 CH_4
Max Power (W/cm^2)	0.007666	0.009884	0.009786	0.008939	0.010815

As mentioned above 50 sccm CH_4 fuel feed and 200 sccm H_2 fuel feed have equavilent reaction capacity towards Ni-YSZ anode surface. But the maximum power of 50 sccm CH_4 fuel feed is lower than 200 sccm H_2 fuel feed. The side reactions taking place when the system is fed with CH_4 fuel decrease the maximum power as in the case of OCV values. The lower maximum power value of 50 sccm CH_4 fuel feed according to 200 sccm H_2 fuel feed and the higher maximum power value of 100 sccm CH_4 fuel feed according to 300 sccm H_2 fuel feed where the system is saturated can be shown as evidence, Figure 3.3.

When the anodic overpotential is applied to the SOFC and started to collect current from the system, maximum power values increase according to the increased fuel concentration. The increasing trend of maximum powers can be seen from Figure 3.3. The anodic overpotential is applied between second and third LSV experiments.

The MEA has both resistive and capacitive properties which can be analyzed through EIS. The Nyquist plot obtained from the EIS provides information about the resistive and capacitive properties. The real part of the impedance (x-axis) indicates the resistive properties and the imaginary part of the impedance (y-axis) indicates capacitive propoperties. Through Nyquist plot the bulk resistances, polarization resistances, and total resistances for different overpotentails for different fuel concentrations can be determined.

From Figure 3.4, the EIS values of 100 sccm H_2 fuel feed for different overpotentials can be determined. The intercept of the x-axis represents the bulk resistances of the MEA at certain overpotentials. Thus, the bulk resistance values for 100 sccm H_2 fuel feed of open circuit voltage (OCV), at 100 mV anodic overpotential, at 200 mV

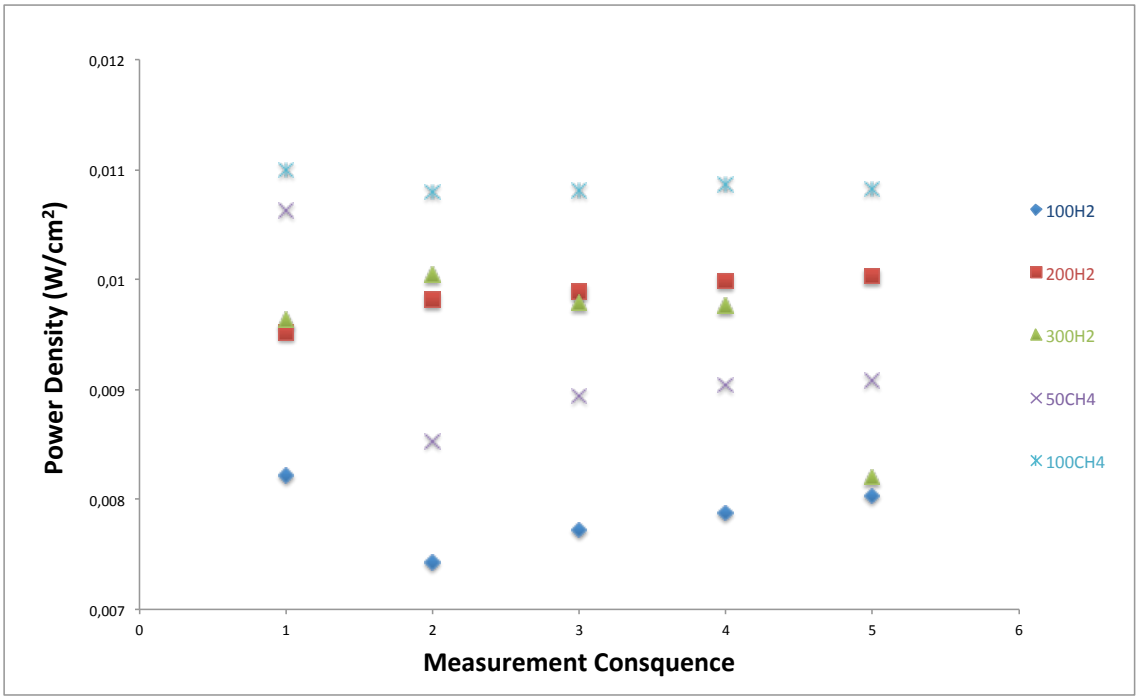


Figure 3.3. Maximum power density values for different fuel concentrations at different stages of measurements.

anodic overpotential and at 300 mV anodic overpotential are 19.3625 Ω cm^2, 19.6250 Ω cm^2, 19.5500 Ω cm^2 and 19.5925 Ω cm^2, respectively.

The bulk resistance increases as overpotential is applied. It is not expected but the increase is in the 5.0 % range quantitavely. Thus, the difference between the bulk resistances due to overpotentail can be neglected. Total resistance is the second intercept of the x-axis which can not be seen from these EIS values. This is basically because of the capacitive properties of the MEA which cannot be monitored in this frequency regime. The polarization resistance which is the difference of total resistance and bulk resistance also can not be seen from these plot. Since we could not determine the total resistance, R_T, the bulk resistances, R_b, are substracted from total resistance.

From Figure 3.5, the EIS values of 200 sccm H_2 fuel feed for different overpotentials can be evaluated. The bulk resistance values for 200 sccm H_2 fuel feed of open circuit voltage (OCV), at 100 mV anodic overpotential, at 200 mV anodic overpotential and at 300 mV anodic overpotential are 19.5775 Ω cm^2, 19.6775 Ω cm^2, 19.7425 Ω

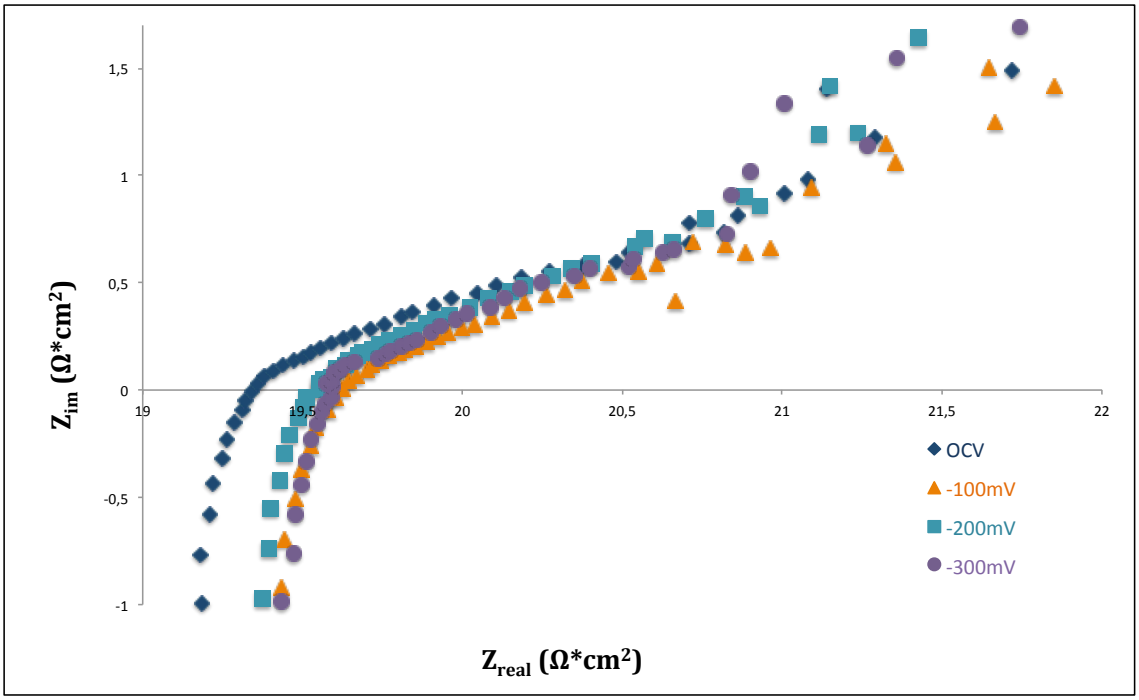


Figure 3.4. Nyquist plots of electrochemical impedance spectroscopy for 100 sccm H_2 at OCV (dark blue), at 100 mV overpotential (orange), at 200 mV overpotential (light blue), and at 300 mV overpotential (purple).

cm^2 and 19.8000 Ω cm^2, respectively.

The bulk resistance is increased as an overpotential is applied and it continues to increase when the applied overpotential is increased. This is not consistent with the previous studies but the differences between bulk resistances are in the 5.0 % range so that they are negligible. Also from this plot the polarization resistance and total resistance can not be determined. The bulk resistances is subtracted and only polarization resistance values are plotted for 200 sccm H_2 concentration fuel feed for further investigation.

From Figure 3.6, the EIS values of 300 sccm H_2 fuel feed for different overpotentials can be determined. The bulk resistance values for 300 sccm H_2 fuel feed of open circuit voltage (OCV), at 100 mV anodic overpotential, at 200 mV anodic overpotential and at 300 mV anodic overpotential are 19.9375 Ω cm^2, 20.1500 Ω cm^2, 20.1725 Ω cm^2 and 20.1100 Ω cm^2, respectively.

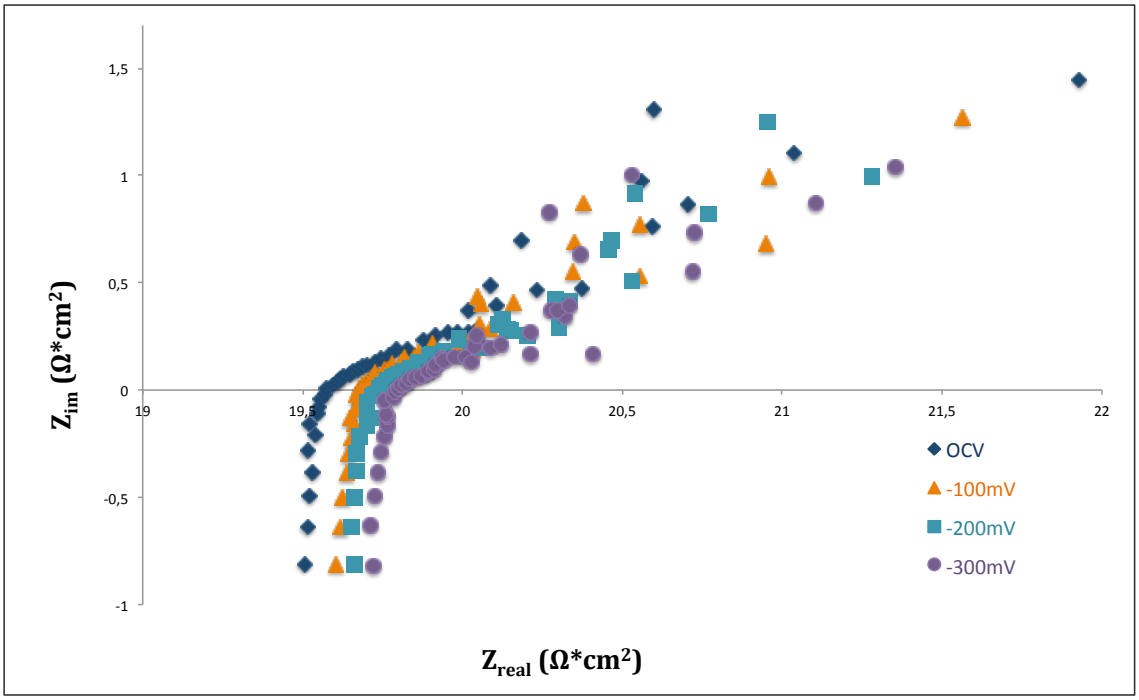


Figure 3.5. Nyquist plots of electrochemical impedance spectroscopy for 200 sccm H_2 at OCV (dark blue), at 100 mV overpotential (orange), at 200 mV overpotential (light blue), and at 300 mV overpotential (purple).

The bulk resistance is increased as an overpotential is applied but it decreased when the applied overpotential is increased. The increase when overpotentail applied is not consistent with the previous studies but the differences between bulk resistances are in the 5.0 % range so that they can be neglected. Also from this plot the polarization resistance and total resistance can not be determined. The bulk resistances are subtracted and only polarization resistance values are plotted for 300 sccm H_2 concentration fuel feed for further investigation.

From Figure 3.7, the EIS values of 50 sccm CH_4 fuel feed for different overpotentials can be seen. The bulk resistance values for 50 sccm CH_4 fuel feed of open circuit voltage (OCV), at 100 mV anodic overpotential, at 200 mV anodic overpotential and at 300 mV anodic overpotential are 20.0750 Ω cm^2, 19.6750 Ω cm^2, 19.6250 Ω cm^2 and 19.7025 Ω cm^2, respectively.

The bulk resistances decrease when anodic overpotential is applied. When the

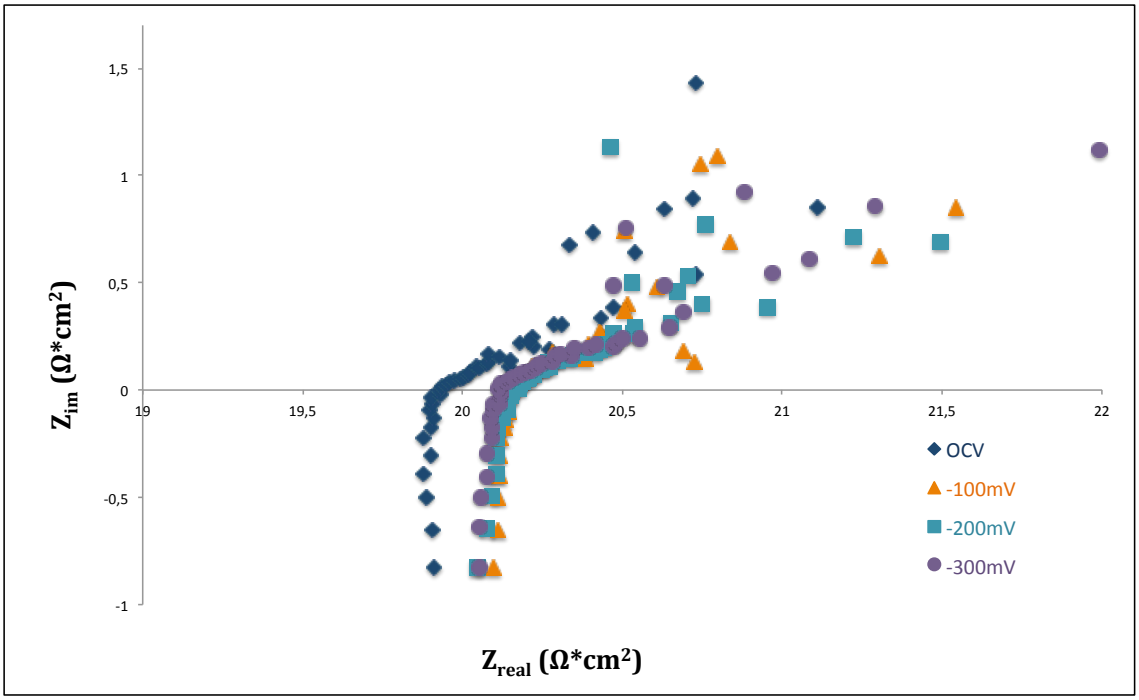


Figure 3.6. Nyquist plots of electrochemical impedance spectroscopy for 300 sccm H_2 at OCV (dark blue), at 100 mV overpotential (orange), at 200 mV overpotential (light blue), and at 300 mV overpotential (purple).

anodic overpotentail is increased from 100 mV to 200 mv the bulk resistance is increased again but when it stepped from 200 mV to 300 mV R_b increases again. As all other deviations are in the 5.0 % range, we could neglect them. Again from this plot the polarization resistance and total resistance can not be evaluated. The bulk resistances are subtracted and only polarization resistance values are plotted for 50 sccm CH_4 concentration fuel feed for further investigation. The MEA is cracked after the experiments. Thus, the post mortem analysis could not provide evidence for carbon deposit since the cathode feed is mixed into anode compartment.

From Figure 3.8, the EIS values of 100 sccm CH_4 fuel feed for different overpotentials can be seen. The bulk resistance values for 100 sccm CH_4 fuel feed of open circuit voltage (OCV), at 100 mV anodic overpotential, at 200 mV anodic overpotential and at 300 mV anodic overpotential are 20.3550 Ω cm^2, 20.6100 Ω cm^2, 20.6650 Ω cm^2 and 20.7475 Ω cm^2, respectively.

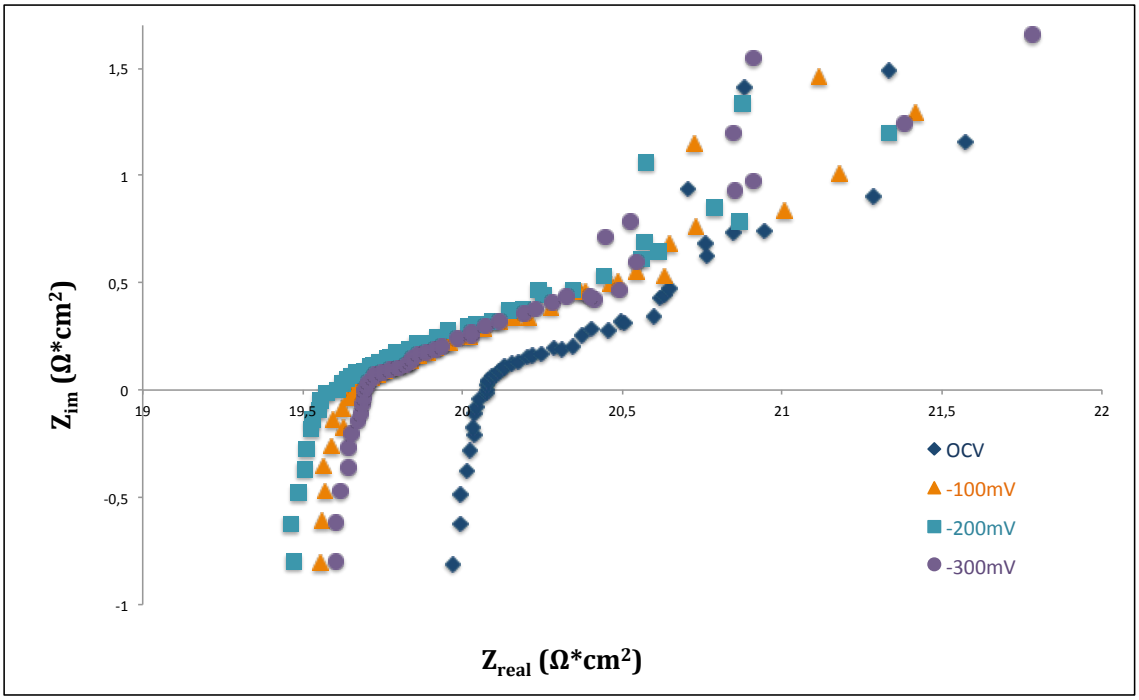


Figure 3.7. Nyquist plots of electrochemical impedance spectroscopy for 50 sccm CH_4 at OCV (dark blue), at 100 mV overpotential (orange), at 200 mV overpotential (light blue), and at 300 mV overpotential (purple).

The bulk resistance is increased as an overpotential is applied and it continue to increase when the applied overpotential is increased. The differences between bulk resistances are in the 5.0 % range so that they can be neglected. Also from this plot the polarization resistance and total resistance can not be evaluated. The bulk resistances is subtracted and only polarization resistance values are plotted for 100 sccm CH_4 concentration fuel feed for further investigation. The MEA is cracked after the experiments. Thus, the post mortem analysis could not provide evidence for carbon deposit since the cathode feed is mixed into anode compartment.

The difference between the bulk resistance and total resistance (two intercepts of x-axis) gives the polarization resistance. Polarization resistances can not be seen clearly from Figures 3.4, 3.5, 3.6, 3.7 and 3.8, so the bulk resistance values are substracted from the Nyquist plots in order to compare the polarization resistances qualitatively and presented in Figures 3.9 and 3.10. Polarization resistances indicate the resistive and capacitive properties of the system due to reactions and processes for fuels.

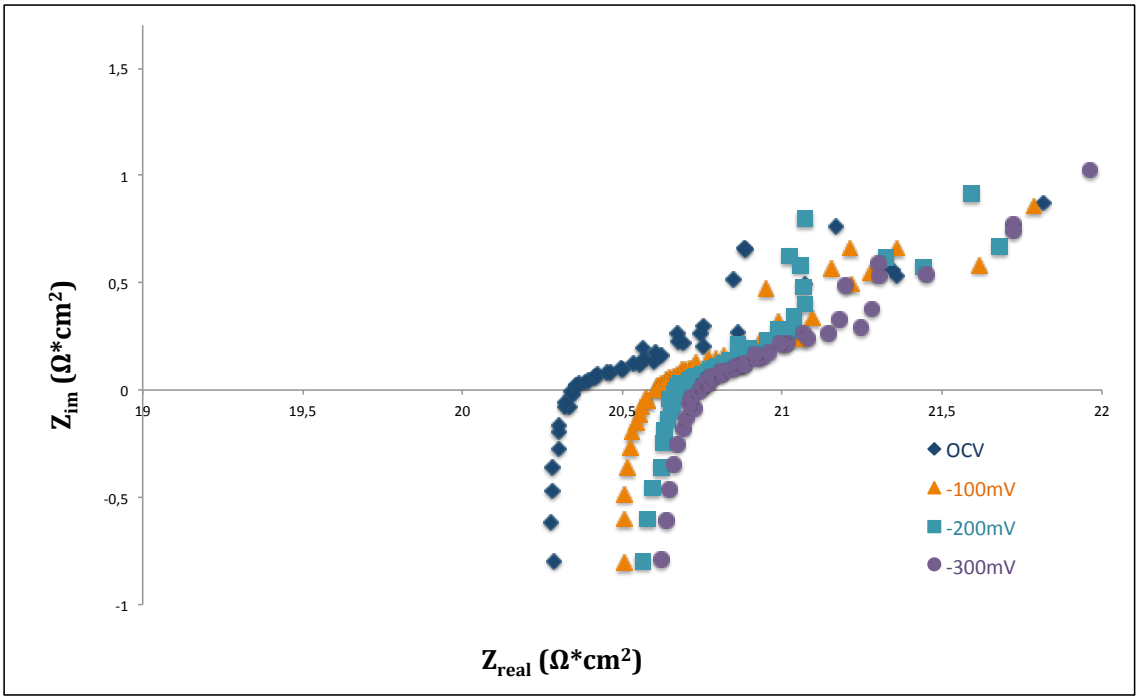
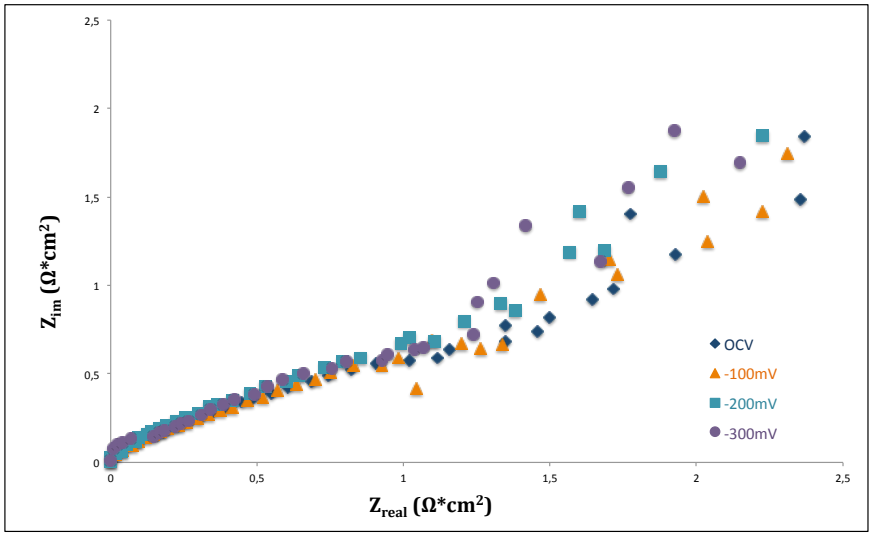


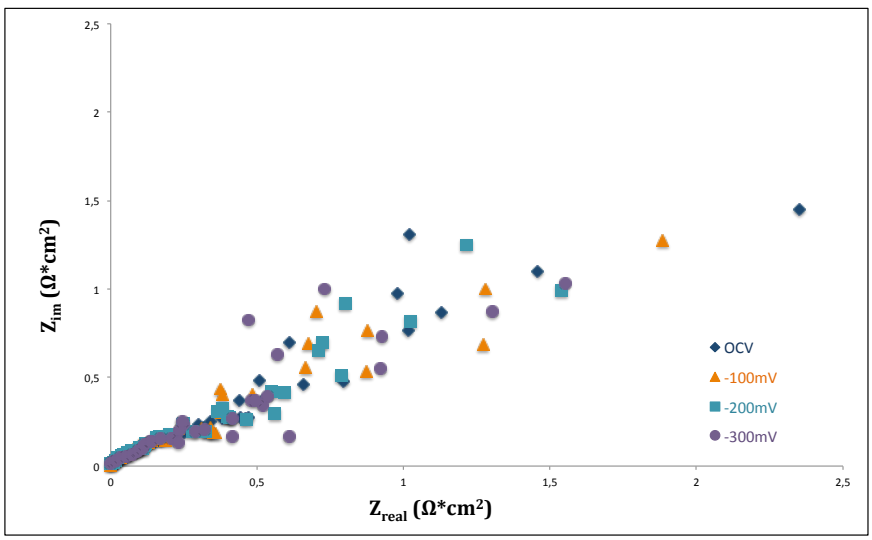
Figure 3.8. Nyquist plots of electrochemical impedance spectroscopy for 100 sccm CH_4 at OCV (dark blue), at 100 mV overpotential (orange), at 200 mV overpotential (light blue), and at 300 mV overpotential (purple).

Increase in the fuel concentration increases the reactions rates and decreases polarization resistances. In Figure 3.9 a, b and c, operations with 100 sccm, 200 sccm and 300 sccm H_2 fuel feed of the MEA is presented and it is obvious that the increase in the H_2 fuel feed concentration decreased the polarization resistance values.

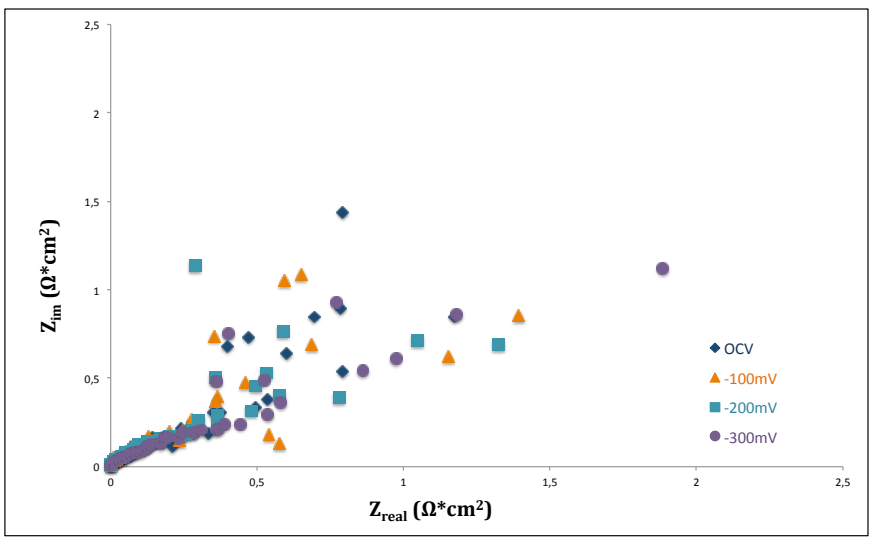
In Figure 3.9 a, the operation with 100 sccm H_2 fuel feed, the polarization resistances are increased when the anodic overpotential is applied and started to collect current. This is basically because of the insufficient amount of fuel and the increase of the polarization resistance due to the increase of the anodic overpotential indicates that the concentration resistance kicks in and effects the polarization resistances. When the MEA is operated with 200 sccm H_2 fuel, Figure 3.9 b, the effect of concentration polarization reduces, thus, the polarization resistances do not change. Increase in the anodic overpotentials do not effect the concentration polarizations, which indicates that there is enough fuel for the full capacity reaction. The polarization resistances of the operation with the 300 sccm H_2 fuel feed, Figure 3.9 c, are exactly as they are supposed to.



(a) 100 sccm H_2 fuel feed

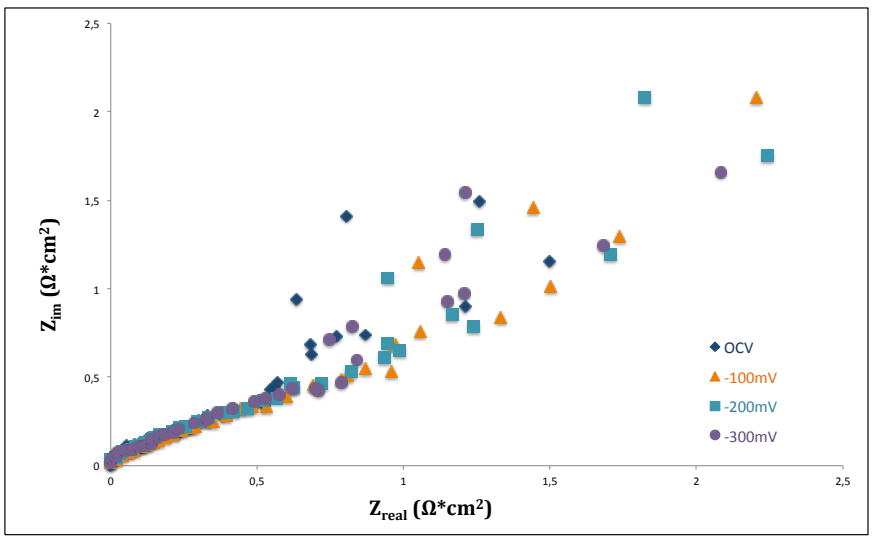


(b) 200 sccm H_2 fuel feed

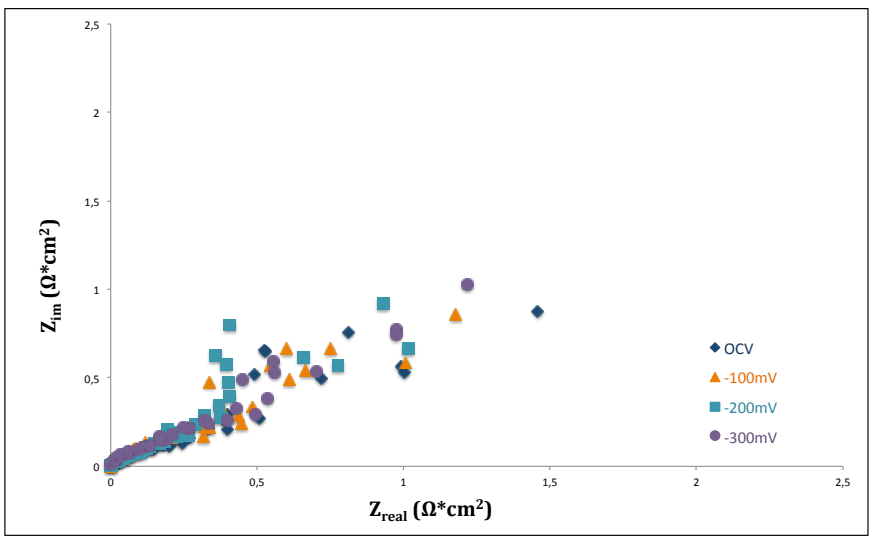


(c) 300 sccm H_2 fuel feed

Figure 3.9. Polarization resistance corrected EIS measurements.



(a) 50 sccm CH_4 fuel feed



(b) 100 sccm CH_4 fuel feed

Figure 3.10. Polarization resistance corrected EIS measurements.

The polarization resistance of the operation with zero anodic overpotential (OCV) is the highest and the resistances decrease as the anodic overpotential is increased. 300 sccm H_2 fuel feed is the optimum fuel feed for the operations.

In Figure 3.10, with the increase of the CH_4 fuel feed concentration, the polarization resistance values decreased. The performance of the MEA with 50 sccm CH_4 fuel feed is similar with 200 sccm H_2 fuel feed in the sense of oxidizing capacity of oxide ions on the anode surface. But there are still distinct differences between them as mentioned above. Thus, the polarization resistance values of 50 sccm CH_4 fuel feed is close but different from 200 sccm H_2 fuel feed. Increase in the applied anodic overpotential decreased the polarization resistances as it supposed to. It can be seen from Figure 3.10 a. In Figure 3.10 b, it can be seen that overall polarization resistances are decreased when the MEA is operated with 100 sccm CH_4 fuel feed. The MEA is cracked after the experiments. Thus, the post mortem analysis could not provide evidence for carbon deposit since the cathode feed is mixed into anode compartment.

The average bulk resistances of the MEA is slightly changed according to the fuel concentrations in time, Table 3.3. The average bulk resistances of 200 sccm H_2 fuel feed and 50 sccm CH_4 fuel feed are again close. Several redox cycles during the operation of the SOFC causes structural changes by effecting the equilibrium condition between Ni and NiO. These changes could be considered as time conditioning of SOFC and could be caused by oxygen leaks through electrolyte into the anode compartment and excess amount of utilized fuel [36, 37]. Time conditioning of the MEA can cause this difference between the bulk resistances of 200 sccm H_2 fuel feed and 50 sccm CH_4 fuel feed as well as H_2 being a better fuel. Hydrogen has high transportation properties and less amount of oxidative reaction variety.

There is no evidence about the carbon deposit on the anode surface of the MEA. There are not any sudden decreases in bulk resistances due to carbon deposit. Even if there is on the anode surface it can not be observed from post mortem analysis since the MEA is cracked. The oxygen feed from cathode is mixed into the anode fuel feed which oxidizes the carbon deposits.

Table 3.3. Bulk resistance values (Ω cm^2) for different fuel concentrations.

Overpotential (mV)	100 H_2	200 H_2	300 H_2	50 CH_4	100 CH_4
OCV	19.3625	19.5775	19.9375	20.0750	20.3550
-100	19.6250	19.6775	20.1500	19.6750	20.6100
-200	19.5500	19.7425	20.1725	19.6250	20.6650
-300	19.5925	19.8000	20.1100	19.7025	20.7475
Average	19.53±0.2	19.70±0.1	20.10±0.2	19.77±0.3	20.59±0.2

3.2. $In-situ$ SOFC Exhaust Analysis

$In-situ$ SOFC exhaust analysis are held by a fuel monitoring system connected directly to the anode exhaust to the SOFC test rig. The transmittance is measured at 2350 nm which is the absorption wavelength of CH_4. The fuel monitoring system is calibrated with CH_4 fuel feed before the measurements. The absoprtion line obtained from the calibration experiments is presented in Figure 2.11. Signals with zero methane concentration taken at the beginning and at the end of the calibration experiments are used to normalize the absorption profile.

Average peak to peak values (Vpp) obtained from the detector via Picoscope digital oscilloscope are used to calculate transmittance of light during the CH_4 measurements and presented in Figures 3.11 and 3.12. In Figure 3.11, the signals are collected during the chronoamperometry experiment with 50 sccm CH_4 fuel feed. The Vpp values and collected current from the SOFC is plotted against time. Collected current at 100 mV and 500 mV are plotted at primary vertical axis and signals from the monitoring system are plotted at secondary axis. The current collected from SOFC system increased from 0.13 A to 0.48 A when the applied anodic overpotential is stepped from 100 mV to 500 mV.

The decrease in the concentration of the absorbing species leads to an increase of the transmitted light. The increase in the signal (Vpp) indicates the decrease of the CH_4 concentration. The signals from monitoring system in Figure 3.11 is increased

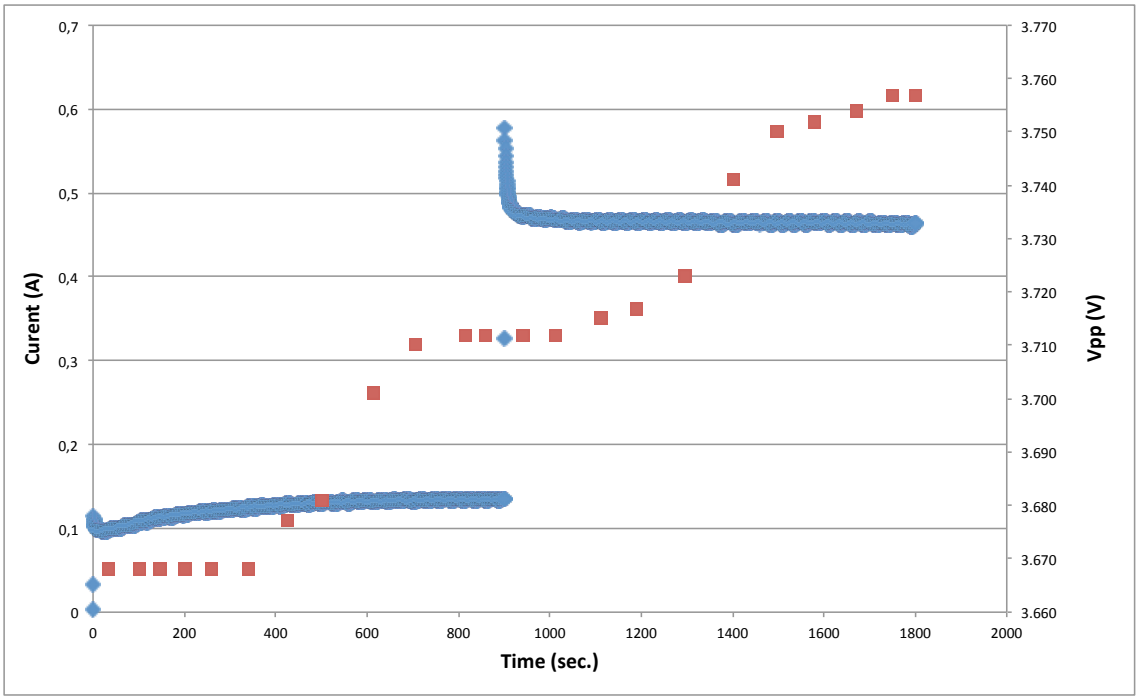


Figure 3.11. $In-situ$ monitoring for 50 sccm CH_4 fuel feed with LED2350 under operating conditions of SOFC.

twice due to the decrease of the CH_4 concentration caused by the two steps of applied anodic overpotential.

The signals in Figure 3.12 are collected during the chronoamperometry experiment with 100 sccm CH_4 fuel feed. The Vpp (peak to peal Voltage) values and collected current from the MEA is plotted against time. Collected current at 100 mV and 500 mV are plotted at primary vertical axis and signals from the monitoring system are plotted at secondary axis. The current collected from SOFC surface increased from 0.08 A to 0.44 A when the applied anodic overpotential is stepped from 100 mV to 500 mV.

The increase in the signal (Vpp) indicates the decrease of the CH_4 concentration. The signals from monitoring system in Figure 3.11 is increased twice due to the decrease of the CH_4 concentration caused by the two steps of applied anodic overpotential.

In Figures 3.13 and 3.14, calculated CH_4 concentrations of insitu SOFC exhaust

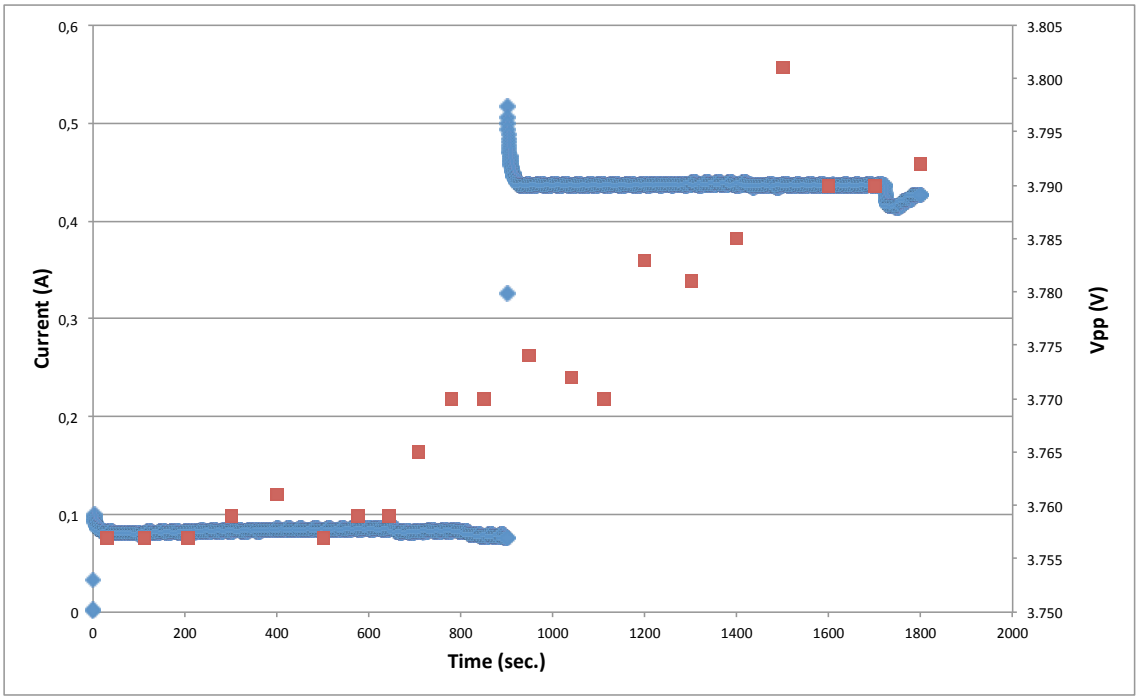


Figure 3.12. $In-situ$ monitoring for 100 sccm CH_4 fuel feed with LED2350 under operating conditions of SOFC.

analysis are presented. Calculated CH_4 concentrations and collected current are plotted against time. The collected current values are presented at primary axis and calculated concentration values are presented at secondary axis.

The signals obtained from the photodetector are used to calculate the transmittance, T. Then, transmittance is employed to calculate the CH_4 concentrations via the Beer-Lambert law (Equation 1.21). The slope of the absorption line is introduced as absoptivity and the path length of the gas cell is 1 cm.

In Figure 3.13, the collected current is increased from 0.13 A to 0.48 A when the applied anodic overpotential is stepped from 100 mV to 500 mV. Actually, there are three steps in this chronoamperometry experiments. Open circuit voltage, 100 mV applied anodic overpotential and 500 mV applied anodic overpotential. 500 mV of applied anodic potential also corresponds to the overpotential that generates maximum power. Thus, there should be two decreasing steps for CH_4 concentration. The first decrease of CH_4 concentration due to 100 mV anodic overpotential starts about 300 seconds after

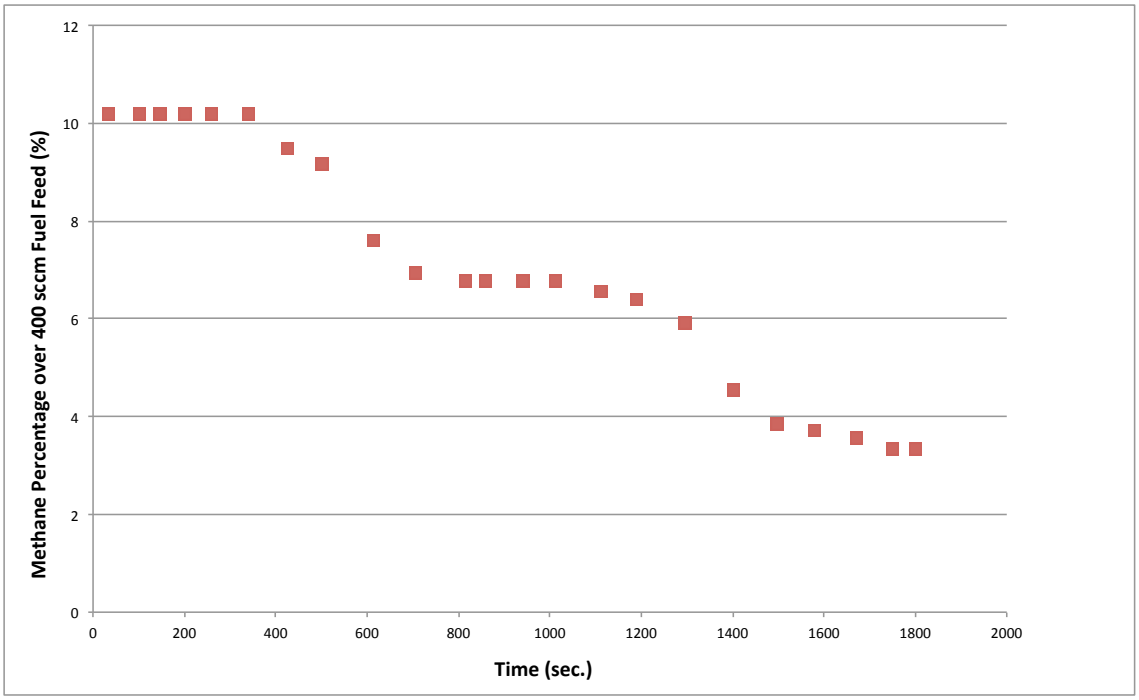


Figure 3.13. $In-situ$ concentration monitoring for 50 sccm CH_4 fuel feed with respect to exhaust gas analysis.

the overpotential is applied and system stabilizes at about 650 to 700 seconds. The second decrease of CH_4 concentration due to 500 mV of anodic overpotential starts again at about 300 seconds after the overpotential is applied and stabilizes at about 650 to 700 seconds.

During the chronoamperometry experiment presented in Figure 3.13 the system is fed with 50 sccm CH_4 corresponding to a 12.5 % CH_4 percentage in the total fuel feed. The first absorption signal indicates that the CH_4 concentration percentage is 10.2 % corresponding to a CH_4 concentration of 40.8 sccm. After the first CH_4 concentration decrease, the absorption signals indicates a CH_4 concentration ratio of 6.8 % corresponding to a CH_4 concentration of 27.2 sccm. After the second CH_4 concentration decrease, the signals indicate a CH_4 concentration percentage of 3.3 % corresponding to a CH_4 concentration of 13.2 sccm.

The fuel conversion efficiency is the conversion percentage of existing electric charge within the fuel into electrical current. For this purpose, fuel conversion effi-

ciencies are calculated as collected electric charge from the SOFC system divided by supplied electric charge within the fuel molecules (Equation 3.1). Supplied electric charge is calculated according to the ideal gas law. In order to find the number of electrons supplied to the system number of moles of fuel molecules consumed during the performance of SOFCs is multiplied by eight donated electrons of one CH_4 molecule (Equation 3.2).

$$Fuel\ Conversion\ Efficiency\ (\%) = \frac{Collected\ electric\ eharge}{Supplied\ electric\ charge} \times 100 \qquad (3.1)$$

$$FCE\ (\%) = \frac{I \times 6.241 \times 10^{18}}{n \times N \times 8} \times 100 \qquad (3.2)$$

Collected electric charge from the SOFCs surface is calculated by converting collected current into electric charge according to Coulomb's law. The fuel conversion efficiencies from the chronoamperometry experiment with 50 sccm CH_4 fuel feed are 11.35 % and 18.57 % for 100 mV and 500 mV overpotentials, respectively.

During the operation with 100 mV anodic overpotential CH_4 consumption is increased by an amount of 13.6 sccm and another 14.0 sccm is started to be consumed during the operation with 500 mV. These increases are directly related with the applied anodic overpotential but the low fuel conversion efficiencies of 11.35 % and 18.57 % and low concentration percentage at the beginning proves that methane undergoes several internal reforming reactions with water vapour and incomplete surface reactions with Ni-YSZ surface.

In Figure 3.14, the collected current is increased from 0.08 A to 0.44 A when the applied anodic overpotential is stepped from 100 mV to 500 mV. The first decrease of

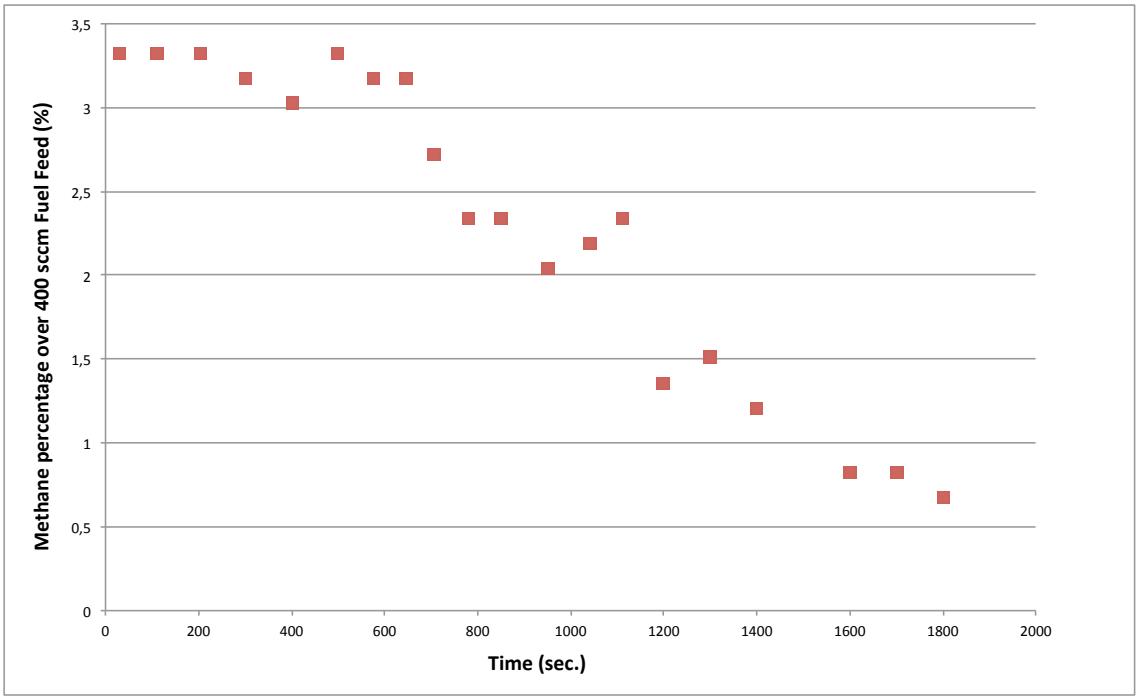


Figure 3.14. $In-situ$ concentration monitoring for 100 sccm CH_4 fuel feed with respect to exhaust gas analysis.

CH_4 concentration due to 100 mV anodic overpotential starts about 300 seconds after the overpotential is applied and system stabilizes at about 650 to 700 seconds. The second decrease of CH_4 concentration due to 500 mV of anodic overpotential starts again at about 300 seconds after the overpotential is applied and stabilizes at about 650 to 700 seconds.

During the chronoamperometry experiment presented in Figure 3.14 the system is fed with 100 sccm CH_4 corresponding to a 25 % CH_4 concentration percentage over the total fuel concentration. The first absorption signal indicates that the CH_4 concentration percentage is 3.3 % corresponding to CH_4 concentration of 13.2 sccm. After the first CH_4 concentration decrease, the absorption signals indicates CH_4 concentration percentage of 2.3 % corresponding to CH_4 concentration of 9.2 sccm. After the second CH_4 concentration decrease, the signals indicate CH_4 concentration percentage of 0.8 % corresponding to CH_4 concentration of 3.2 sccm.

The fuel conversion efficiencies from the chronoamperometry experiment with

100 sccm CH_4 fuel feed are 1.09 % and 5.35 % for 100 mV and 500 mV overpotentials, respectively.

During the operation with 100 mV anodic overpotential the CH_4 consumption is increased by an amount of 4.0 sccm and another 6.0 sccm is started to be consumed during the operation with 500 mV.

In the chronoamperometry experiment with 100 sccm CH_4 fuel feed, there are several indications that the MEA is cracked. Besides the fuel conversion efficiencies are being very low, the amount of CH_4 consumption at the beginnig of the experiment is very high but a very small increase occured in the CH_4 consumption when the overpotential is stepped. Moreover, the sudden drop at the end of the current line in Figure 3.14 indicates cracking on the MEA.

4. CONCLUSIONS

In this study, SOFC operating with syngas and coal gasification integrated system is designed and developed. The effects of fuel concentration on the SOFCs' performance are investigated. Different fuel concentrations of H_2 and CH_4 are analyzed electrochemically and analytically. Cathode compartment of SOFC is fed with O_2 by the rate of 400 sccm. On the other side of the SOFC, anode compartment is fed with the flow rate of 400 sccm fuel mixture. Fuel mixtures are composed of 100 sccm, 200 sccm, 300 sccm H_2 and 50 sccm, 100 sccm CH_4, all of which completed to 400 sccm with N_2 as diluent gas.

Performance analysis of the SOFC operating with different fuel concentrations are evaluated by elecrochemical methods. Linear sweep voltammetry method is used to compare the differences between OCV and power output values for different fuel concentrations. EIS is used to analyze the resistive and capacitive properties of the SOFC system. The effects of different fuel concentrations are mostly observed as changes in the polarization resistances.

$In-situ$ exhaust analysis of the SOFC with different fuel concentrations are monitored by simultaneous experiments of chronoamperometry and mid-IR absorption spectroscopy. Fuel conversion efficiency values of SOFC system are calculated for different CH_4 fuel concentrations at various overpotentials. $In-situ$ exhaust analysis can only be applied to CH_4 fuel concentrations since H_2 molecules are not large enough to detect by mid-IR absorption spectroscopy.

Open circuit voltage value of 0.963 V shows that the surface reactions are reached to dynamic equilibrium when the SOFC is fed with 200 sccm H_2 fuel feed. Eventhough 200 sccm H_2 fuel feed is equivalent to 50 sccm CH_4 fuel feed in terms of oxidation capacity towards transported oxide ions from cathode to anode, reactions on the Ni-YSZ anode surface do not reach to equilibrium with 50 sccm CH_4 fuel feed. Thus, 100 sccm CH_4 fuel leads to a higher open circuit voltage value as 1.03 V.

A comparison between the maximum power values of different H_2 fuel concentrations indicates that the system is saturated towards H_2 fuel feed at 200 sccm. The maximum power values of 200 sccm and 300 sccm H_2 fuel feeds are the same. Hence, the system is not saturated by 50 sccm CH_4 fuel feed and the maximum power value of 100 sccm CH_4 fuel feed is higher than both 50 sccm CH_4 fuel feed and 200 sccm H_2 fuel feed.

EIS measurements indicate the bulk resistance and polarization resistance of the SOFC system. Changes in the bulk resistances are insignificant for all fuel concentrations within a deviation range of 5.0 %. Polarization resistances are related with the concentration polarization of the SOFC system. All of the concentration polarizations for different fuel mixture decrease with the increase of the fuel concentrations. Polarization resistances also indicate that there is enough fuel for full capacity of SOFC system above 200 sccm H_2 fuel feed.

Low fuel conversion efficiencies of CH_4 calculated from the results of simultaneous experiments of chronoamperometry and mid-IR absorption spectroscopy is addressed that methane undergoes indirect oxidation besides direct oxidation on SOFC anode surface during the internal reforming. Side reactions of methane and their byproducts might also increase the stress on MEA and shorten the life time of the SOFC.

According to these results, it can be evaluated that H_2 is a better fuel comparing to CH_4 for SOFCs with its high mobility and less reactivity against water vapor produced on the anode surface. On the other hand, the fuel conversion efficiency of CH_4 is 18.57 % for 50 sccm CH_4 fuel feed at 500 mV anodic overpotential during the SOFCs operation. These results for CH_4 fuel are promising in the matter of designing of SOFC operating with syngas and coal gasification integrated system.

5. FUTURE WORKS

Experiments held for SOFC with single stack configuration will be repeated for SOFC with multiple stack configuration. Performance analysis of SOFCs with multiple stack configurations will address whether the fuel conversion efficiencies increase with increasing MEA surface area or not.

Coal gasification experiments will be held by coal gasification reactor. Necessary purification of the generated coal syngas will be done in two steps. Cyclone filter will be the first step and remove the large sized particles such as tar. Porous silicate metarial placed at the outlet of the cyclone filter will hold the small size impurities such as Cl, Sb, As, P... Concentration analysis of the coal gasification will be managed by $in-situ$ monitoring with the fuel monitoring system. H_2O could be fed to the reactor through MFCs and directly from the exhaust of the SOFC. Direct feed of H_2O from the exhaust of the SOFC to coal gasification will require a CO_2 sequestration step. CO_2 sequestration will be achieved by a sequestration unit composed of $Ca(OH)_2$. Utilization of the existing coal gasification reactor will enable the direct feed of coal syngas to the SOFC. Thus, long-term operation stablity of SOFC operating with syngas and coal gasification integrated system could be evaluated.

LEDs with different wavelengths will be integrated to have a multicomponent gas analysis. Fuel monitoring system has the infrastructure for the utilization of multiple LEDs with different wavelengths. Driving signals for LEDs with different central wavelengths will be optimized and those LEDs will also be included to the fuel monitoring system. Calibration experiments for LEDs with 1900 nm, 2050 nm, 4300 nm, and 4600 nm central wavelengths will be done. Rotating stage will enable to have absorption detection with different LEDs from the same sample line. Measurements with multiple LEDs could be included to the multicomponent gas analysis calculations. Thus, concentrations H_2O, CO, CO_2 could also be evaluated quantitatively.

REFERENCES

1. Atkins, P., and J. Paula, *Physical Chemistry*, Oxford University Press, Oxford, 2002.

2. Lundberg, W.L., S.E. Veyo, and M.D. Moeckel, "A High-Hfficiency Solid Oxide Fuel Cell Hybrid Power System Using the Mercury 50 Advanced Turbine Systems Gas Turbine", *Journal Of Engineering For Gas Turbines And Power- Transactions Of The Asme*, Vol. 125, No. 1, pp. 51-58, 2003.

3. Jayanti, S.,V. Prabu, "Underground Coal-Air Gasification Based Solid Oxide Fuel Cell System", *Applied Energy*, Vol. 94, pp. 406–414, 2012.

4. Ormerod, R.M., "Solid Oxide Fuel Cells", *Chemical Society Reviews*, Vol.32, No. 1, pp. 17-28, 2003.

5. Nernst, W., "Uber die Elektrolytische Leitung Fester Korper bei Sehr Hohen Temperaturen", *Z. Elektrochem.*, Vol. 6, pp. 41, 1899.

6. Grove, W.R., "On Voltaic Series and the Combination of Gases by Platinum", *Philosophical Magazine*, Vol. 14, pp. 127, 1839.

7. W.Nernst, *patent D.R.P. 104872*, 1897.

8. Baur, E., H. Preis, "Über Brennstoff-Ketten mit Festleitern", *Zeitschrift für Elektrochemie und Angewandte Physikalische Chemie*, Vol. 43, No. 9, pp. 727, 1937.

9. Brandon, N.P., S. Skinner, and B.C.H. Steele, "Recent Advances in Materials for Fuel Cells", *Annual Review Of Materials Research*, Vol. 33, pp. 183-213, 2003.

10. Ormerod, R.M., "Solid Oxide Fuel Cells", *Chemical Society Reviews*, Vol. 32, No. 1, pp. 17-28, 2003.

11. Florio, D. Z., F. C. Fonseca, E. N. S. Muccillo, "Ceramic Materials for Fuel Cells",

Cerâmica, Vol. 50, No. 316, pp. 275-290, 2004.

12. Holtappels, P., U. Vogt, and T. Graule, "Ceramic Materials for Advanced Solid Oxide Fuel Cells", *Advanced Engineering Materials*, Vol. 7, No. 5, pp. 292-302, 2005.

13. Fergus, J.W., "Electrolytes for Solid Oxide Fuel Cells", *Journal Of Power Sources*, Vol. 162, No. 1, pp. 30-40, 2006.

14. Lee, T. S., J.N. Chung, Y. C. Chen, "Design and Optimization of a Combined Fuel Reforming and Solid Oxide Fuel Cell", *Energy Conversion and Managment*, Vol. 52, pp 3214- 3226, 2011.

15. He, H.P., J.M. Hill, "Carbon Deposition on Ni/YSZ Composites Exposed to Humidified Methane." *Applied Catalysis A-General*, Vol. 317, pp 284-292, 2007.

16. Putna, E.S., J. Stubenrauch , J. M. Vohs , R. J. Gorte., "Ceria-Based Anodes for the Direct Oxidation of Methane in Solid Oxide Fuel Cells", *Langmuir*, Vol. 11, No. 12, pp. 4832-4837, 1995.

17. Sin, A., E. Kopnin, Y. Dubitsky, A. Zaopo, A.S. Aricò, D. La Rosa, L.R. Gullo, V. Antonucci, "Performance and Life-Time Behaviour of NiCu-CGO Anodes for the Direct Electro-Oxidation of Methane in IT-SOFCs", *Journal Of Power Sources*, Vol. 164, No. 1, pp. 300-305, 2007.

18. Liu, J., B. D. Madsen, Z. Ji, and S. A. Barnett, "A Fuel-Flexible Ceramic-Based Anode for Solid Oxide Fuel Cells", *Electrochemical And Solid State Letters*, Vol. 5, No 6, pp. A122-A124, 2002.

19. Sauvet, A.L., J. Fouletier, "Catalytic Properties of New Anode Materials for Solid Oxide Fuel Cells Operated Under Methane at Intermediary Temperature", *Journal Of Power Sources*, Vol. 101, No. 2, pp. 259-266, 2001.

20. Hattori, M., Y. Takeda, Y. Sakaki, A. Nakanishi, S. Ohara, K. Mukai, J. Lee, T.

Fukui, "Effect of Aging on Conductivity of Yttria Stabilized Zirconia", *Journal Of Power Sources*, Vol. 126, No. 1-2, pp. 23-27, 2004.

21. Goodenough, J.B., "Oxide-Ion Electrolytes", *Annual Review Of Materials Research*, Vol. 33, pp. 91-128, 2003.

22. Luo, J., R.J. Ball, and R. Stevens, "Gadolinia Doped Ceria/Yttria Stabilised Zirconia Electrolytes for Solid Oxide Fuel Cell Applications", *Journal Of Materials Science*, Vol. 39, No. 1, pp. 235-240, 2004.

23. Maguire, E., B. Gharbage, F.M.B Marques, J.A Labrincha, "Cathode Materials for Intermediate Temperature SOFCs", *Solid State Ionics*, Vol. 127, pp 329-335, 2000.

24. Sun, C., R. Hui, J. Roller, "Cathode Materials for Solid Oxide Fuel Cells: a Review", *Solid State Electrochem* , Vol. 14, pp 1125-1144, 2010.

25. Jørgensen , M.J., S. Primdahl, C. Bagger, M. Mogensen, "Effect of Sintering Temperature on Microstructure and Performance of LSM–YSZ Composite Cathodes", *Solid State Ionics*, Vol. 139, pp 1-11, 2001.

26. Hwang, H.J., J.W. Moon, S. Lee, E. A. Lee, "Electrochemical Performance of LSCF-Based Composite Cathodes for Intermediate Temperature SOFCs", *Journal Of Power Sources*, Vol. 145, No. 2, pp. 243-248, 2005.

27. Wang, W.G., M. Mogensen, "High-Performance Lanthanum-Ferrite-Based Cathode for SOFC", *Solid State Ionics*, Vol. 176, No. 5-6, pp. 457-462, 2005.

28. Yokokawa, H., Sakai, N., Horita, T., Yamaji, K., "Investigation of $La_{1-x}Sr_xCrO_{3-\partial}$ as Membrane for Hydrogen" *Fuel Cells*, Vol. 1, No. 2: pp. 117, 2001.

29. Bard, A.J., L.R. Faulkner, "Electrochemical Methods: Fundamentals and Applications", 2nd ed, *John Wiley*, 2001.

30. Larminie, J.D., "Fuel Cell Systems Explained", *Wiley*, New York, 2001.

31. Barsoukov, E.M., R. J., "Impedance Spectroscopy: Theory, Experiment, and Applications", *Wiley*, New York, 2005.

32. Bessler, W. G., J. Warnatz, D. G. Goodwin, "The Influence of Equilibrium Potential on the Hydrogen Oxidation Kinetics of SOFC Anodes", *Solid State Ionics*, Vol. 177, pp. 3371–3383, 2007.

33. Mogensen, M. and K. Kammer, "Conversion of Hydrocarbons in Solid Oxide Fuel Cells". *Annual Review of Materials Research*, Vol. 33, pp. 321-331, 2003.

34. Liese, E. A., Gemmen, R. S.,Performance Comparison of Internal Reforming Against External Reforming in a Solid Oxide Fuel Cell, Gas Turbine Hybrid System", *Journal fo Engineering for Gas Turbines Power*, Vol. 127, No.1, pp. 86-127, 2005.

35. Varshney, P.,M. K. Mondal, H. K. Balsora, "Progress and Trends in CO_2 Capture/Separation Technologies: A Review", *Energy*, Vol. 46, pp. 431-441, 2012.

36. Ettler, M., H. Timmermann, J. Malzbender, A. Weber, N. H. Menzler, "Durability of Ni anodes during reoxidation cycles",*Journal of Power Sources*, Vol. 195, No. 17, pp. 5452-5467, 2010.

37. Sarantaridis, D., A. Atkinson, "Redox Cycling of Ni-Based Solid Oxide Fuel Cell Anodes: A Review", *Fuel Cells*, Vol. 7, pp. 246, 2007.

38. Cayana, F.N., M. Zhia, S. R. Pakalapatia, I. Celika, N. Wua, R. Gemmenb, "Effects of Coal Syngas Impurities on Anodes of Solid Oxide Fuel Cells", *Journal of Power Sources*, Vol. 185, pp. 595–602, 2008.

39. Yoshiie, R., Y. Taya, T. Ichiyanagi , Y. Ueki , I. Naruse, "Emissions of Particles and Trace Elements from Coal Gasification", *Fuel*, Vol. 108, pp. 67–72, 2013.

40. Johnstone, W., M. Lengdena, R. Cunningham, "Tuneable Diode Laser Gas Anal-

yser for Methane Measurements on a Large Scale Solid Oxide Fuel Cell", *Journal of Power Sources*, Vol. 196, pp. 8406–8408, 2011.

41. L.S. Rothman, I.E. Gordon, A. Barbe, D. Chris Benner, P.F. Bernath, M. Birk, V. Boudon, L.R. Brown, A. Campargue, J.-P. Champion, K. Chance, L.H. Coudert, V. Dana, V.M. Devi, S. Fally, J.-M. Flaud, R.R. Gamache, A. Goldman, D. Jacquemart, I. Kleiner, N. Lacome, W.J. Lafferty, J.-Y. Mandin, S.T. Massie, S.N. Mikhailenko, C.E. Miller, N. Moazzen-Ahmadi, O.V. Naumenko, A.V. Nikitin, J. Orphal, V.I. Perevalov, A. Perrin, A. Predoi-Cross, C.P. Rinsland, M. Rotger, M. Simeckovo, M.A.H. Smith, K. Sung, S.A. Tashkun, J. Tennyson, R.A. Toth, A.C. Vandaele, J. Vander Auwera, "The HITRAN 2008 Molecular Spectroscopic Database", *J. Quant. Spectrosc. Ra.*, Vol. 110, pp. 533–572, 2009.

42. Hanson, R. K., R. Sur, K. Sun, J. B. Jeffries, J. G. Socha, "Scanned-Wavelength-Modulation-Spectroscopy Sensor for CO, CO_2, CH_4 and H_2O in a High-Pressure Engineering-Scale Transport-Reactor Coal Gasifier", *Fuel*, Vol. 150,pp. 102–111, 2015.